

# **Powerful Shocks and Cavities in the Hot Atmosphere of the MS 0735 Galaxy Cluster**

by

Adrian Vantyghem

A thesis  
presented to the University of Waterloo  
in fulfillment of the  
thesis requirement for the degree of  
Master of Science  
in  
Physics

Waterloo, Ontario, Canada, 2014

© Adrian Vantyghem 2014

## **Author's Declaration**

I hereby declare that I am the sole author of this thesis. This is a true copy of the thesis, including any required final revisions, as accepted by my examiners. The majority of this thesis, Chapters 2 – 6, has been published as:

- *Cycling of the powerful AGN in MS 0735.6+7421 and the duty cycle of radio AGN in clusters*, A. N. Vantyghem, B. R. McNamara, H. R. Russell, R. A. Main, P. E. J. Nulsen, M. W. Wise, H. Hoekstra, and M. Gitti, 2014, MNRAS, 442:31923205.

I understand that my thesis may be made electronically available to the public.

## Abstract

Cool core clusters host bright centres that radiate away their energy in less than  $10^9$  yr. If uncompensated by heating, the hot atmosphere will cool and form stars at rates of hundreds to thousands of solar masses per year. However, high resolution spectroscopy from the *Chandra* and *XMM-Newton* X-ray Observatories have failed to find evidence of gas cooling to low temperatures at the expected rates. Instead, feedback from active galactic nuclei (AGN) is heating the intracluster medium and suppressing cooling flows. X-ray observations have revealed large cavities, weak shocks, and sound waves in the intracluster medium that are produced by the relativistic jets launched by the central AGN.

In this thesis I present a deep *Chandra* X-ray analysis of MS 0735.6+7421 (MS0735), the cool core galaxy cluster with the most energetic AGN outburst known. I use this deep observation to study the energetics of the powerful AGN outburst, as well as analyze additional effects that the outburst has on the intracluster medium. Two large cavities, with diameters of 200-240 kpc, are embedded in the hot atmosphere of MS0735. A power output of over  $10^{46}$  erg s<sup>-1</sup> is required to inflate the bubbles, exceeding the X-ray luminosity by over a factor of 60 and easily offsetting radiative losses. A continuous, weak shock front of Mach number 1.26 encompasses the cavities, injecting energy at a rate comparable to the cavities. This shock causes a temperature jump that varies azimuthally, and is highest where the shock front is strongest. Cool gas from the centre of the cluster is entrained in the radio jet and is being dragged toward high altitudes. Two more cavities are observed near the cluster centre, indicating that the AGN is rejuvenating on a timescale shorter than the central cooling time. These cavities, while small compared to the older outburst, still contain ample energy to offset radiative losses.

With the addition of MS0735, I prepare a sample of 10 clusters and groups with multiple generations of cavities. Three systems with detected sound waves are also included, two of which overlap with the cavity sample. In these systems I compare the mean time interval between AGN outbursts to the central cooling time and cavity heating time. On average the AGN rejuvenate on a timescale that is approximately 1/3 of their mean central cooling time, indicating that jet heating is outpacing cooling in these systems.

Finally, I present a preliminary analysis of integral field spectroscopy of MS0735's brightest cluster galaxy. A velocity gradient extends across the cluster nucleus and is inconsistent with being a rotating disk. Instead, it is more likely that the atomic gas has been entrained in the jets and is being dragged away from the nucleus. The ionized gas mass exceeds estimates based on the upper limits of molecular gas, indicating either that the atomic gas is not condensing into molecular gas or that a source of heat is reionizing the H $\alpha$  nebula.

## **Acknowledgements**

I would like to thank all the people who made this thesis possible: my supervisor, Prof. Brian McNamara, for his guidance and assistance in the completion of this thesis; Dr. Helen Russell, for her endless patience and support; Robert Main, for many interesting conversations; my collaborators, Paul Nulsen, Michael Wise, Henk Hoekstra, Myriam Gitti, and Julie Hlavacek-Larrondo, for their insightful comments; my friends, for all the good times; my family, for their continued support; and Laura, for being with me every step of the way.

# Table of Contents

|  |             |
|--|-------------|
| <b>List of Tables</b>                              | <b>viii</b> |
| <b>List of Figures</b>                             | <b>ix</b>   |
| <b>1 Introduction</b>                              | <b>1</b>    |
| 1.1 Intracluster Medium . . . . .                  | 2           |
| 1.2 Cooling Flows . . . . .                        | 3           |
| 1.3 Feedback from Active Galactic Nuclei . . . . . | 4           |
| 1.3.1 X-ray Cavities . . . . .                     | 4           |
| 1.3.2 Weak Shocks and Sound Waves . . . . .        | 7           |
| 1.3.3 Powering AGN Outbursts . . . . .             | 8           |
| 1.3.4 Metal-Enriched Outflows . . . . .            | 9           |
| 1.3.5 Repeated Outbursts . . . . .                 | 10          |
| 1.4 MS 0735.6+7421 . . . . .                       | 11          |
| <b>2 Observations and Data Reduction</b>           | <b>13</b>   |
| <b>3 Cluster X-ray Properties</b>                  | <b>16</b>   |
| 3.1 Surface Brightness . . . . .                   | 16          |
| 3.2 Projected Profiles . . . . .                   | 17          |
| 3.2.1 Spectral Fitting . . . . .                   | 19          |

|          |  |           |
|----------|--|-----------|
| 3.2.2    | Temperature Profile . . . . .                          | 19        |
| 3.2.3    | Abundance Profile . . . . .                            | 21        |
| 3.2.4    | Entropy Profile . . . . .                              | 21        |
| 3.2.5    | Cooling Time . . . . .                                 | 21        |
| 3.3      | Deprojected Profiles . . . . .                         | 23        |
| 3.4      | Maps . . . . .   | 24        |
| 3.4.1    | Temperature Map . . . . .                              | 24        |
| 3.4.2    | Abundance Map . . . . .                                | 27        |
| 3.5      | Multiphase Gas . . . . .                               | 27        |
| 3.6      | Cooling Region . . . . .                               | 29        |
| <b>4</b> | <b>The Powerful AGN Outburst</b>                       | <b>30</b> |
| 4.1      | Cavities . . . . .                                     | 30        |
| 4.2      | Cavity Rims . . . . .                                  | 32        |
| 4.3      | Shock . . . . .  | 33        |
| <b>5</b> | <b>Rejuvenated Outburst</b>                            | <b>38</b> |
| 5.1      | Spectrally Hard Features: An Inner Shock? . . . . .    | 41        |
| <b>6</b> | <b>AGN Outburst Time Dependence</b>                    | <b>42</b> |
| <b>7</b> | <b>Optical</b>   | <b>47</b> |
| 7.1      | Observations . . . . .                                 | 48        |
| 7.2      | Data Reduction . . . . .                               | 48        |
| 7.3      | Spectral Fitting . . . . .                             | 50        |
| 7.4      | Maps . . . . .   | 52        |
| 7.5      | Ordered Motion . . . . .                               | 54        |
| 7.5.1    | Rotation . . . . .                                     | 56        |
| 7.5.2    | Entrainment . . . . .                                  | 58        |
| 7.6      | Motion Induced by an Ultramassive Black Hole . . . . . | 59        |
| 7.7      | Mass Estimates . . . . .                               | 59        |

|          |                            |           |
|----------|----------------------------|-----------|
| <b>8</b> | <b>Conclusions</b>         | <b>61</b> |
| 8.1      | Summary . . . . .          | 61        |
| 8.2      | Future Work . . . . .      | 63        |
|          | <b>APPENDICES</b>          | <b>65</b> |
| A        | <b>Other Contributions</b> | <b>66</b> |
|          | <b>References</b>          | <b>68</b> |

# List of Tables

|     |  |    |
|-----|--|----|
| 2.1 | Exposure Times. . . . .                                | 14 |
| 4.1 | List of cavity properties. . . . .                     | 31 |
| 6.1 | Sample of systems with multiple AGN outbursts. . . . . | 43 |

# List of Figures

|     |   |    |
|-----|---|----|
| 1.1 | Composite image of MS0735. . . . .  | 11 |
| 2.1 | X-ray image of MS0735 . . . . .   | 15 |
| 3.1 | Cluster surface brightness profile fit with a double-beta model . . . . .   | 17 |
| 3.2 | Residual surface brightness after subtracting a double-beta model . . . . . | 18 |
| 3.3 | Projected radial profiles . . . . .   | 20 |
| 3.4 | Deprojected radial profiles . . . . .                                       | 22 |
| 3.5 | Map of gas temperature and metal abundance . . . . .                        | 25 |
| 3.6 | Entrainment of central gas in the radio jet . . . . .                       | 26 |
| 3.7 | Soft excess in the spectrum of the central region . . . . .                 | 27 |
| 4.1 | Bright emission from cavity rim . . . . .                                   | 33 |
| 4.2 | Surface brightness profile across the shock front . . . . .                 | 34 |
| 4.3 | Azimuthal dependence of post-shock temperature . . . . .                    | 36 |
| 5.1 | Image of the 0.3-1 keV surface brightness . . . . .                         | 39 |
| 5.2 | Image of the 3-7 keV surface brightness . . . . .                           | 40 |
| 6.1 | Outburst interval compared to central cooling time . . . . .                | 45 |
| 6.2 | Outburst interval compared to cavity heating time . . . . .                 | 46 |
| 7.1 | Optical spectrum of the brightest cluster galaxy . . . . .                  | 50 |

|     |   |    |
|-----|---|----|
| 7.2 | Sample fit to the $H\alpha$ and [NII] lines of the optical spectrum . . . . . | 51 |
| 7.3 | Continuum and $H\alpha$ flux maps . . . . .                                   | 53 |
| 7.4 | Velocity maps of the gaseous nebula . . . . .                                 | 55 |
| 7.5 | Map of velocity dispersion . . . . .  | 56 |
| 7.6 | Velocity gradient of the $H\alpha$ nebula . . . . .                           | 57 |

# Chapter 1

## Introduction

Clusters of galaxies are the largest gravitationally bound structures in the Universe. At optical wavelengths they are characterized by overdensities in the distribution of galaxies on the sky (Wolf, 1906), and typically contain hundreds of individual galaxies spread over a spatial region several Mpc in diameter. One galaxy typically dominates the others in terms of mass and luminosity. This galaxy is termed the brightest cluster galaxy (BCG), and normally resides within a few kpc of the centre of the gravitational potential well.

Galaxy clusters have masses in the range of  $10^{14} - 10^{15} M_{\odot}$ , only a few percent of which is contained in galaxies. A hot, diffuse plasma, called the intracluster medium (ICM), permeates the cluster and accounts for an additional  $\sim 13\%$  of its total mass. Launched in 1970, the *Uhuru* satellite allowed the sky to be surveyed at X-ray frequencies (Giacconi et al., 1972; Kellogg et al., 1971, 1973), leading to the detection of the ICM in over 40 galaxy clusters (Gursky & Schwartz, 1977), with typical X-ray luminosities of  $10^{43} - 10^{45} \text{ erg s}^{-1}$ . Later analysis with the *Ariel-5* (Mitchell et al., 1976) and *OSO-8* (Serlemitsos et al., 1977) observatories revealed a 6 – 7 keV Fe-K emission line, indicating that the X-ray emission originates from a thermal plasma with temperatures between  $10^7 - 10^8$  K. This thermal plasma is in hydrostatic equilibrium, tracing the potential well of the gravitating mass.

The vast majority of the mass in clusters ( $\sim 85\%$ ) is contained in non-baryonic (dark) matter that only interacts gravitationally. Since dark matter comprises the majority of the cluster's mass, the shape of the gravitational potential well is dictated by the distribution of dark matter. Clear evidence of dark matter is seen in the Bullet cluster, a merging system where the baryonic matter is clearly separated from the gravitational potential well as determined through weak lensing (Clowe et al., 2004, 2006).

## 1.1 Intracluster Medium

The intracluster medium (ICM) consists mainly of primordial hydrogen and helium that was swept into the dark matter halo as the cluster was being formed. Metals, with an abundance of roughly 1/3 solar, also provide a small contribution to the total ICM mass (Edge & Stewart, 1991). The virialized gas, at temperatures of  $10^7 - 10^8$  K, is almost entirely ionized. Consistency between the mean gas temperature and velocity dispersion of cluster galaxies,  $\sigma$ , through the relation  $T \propto \sigma^2$  (Mushotzky et al., 1978) indicates that galaxy clusters are relaxed systems with galaxies and hot baryons responding to the same gravitational potential. Gas density, which ranges between  $10^{-4} \text{ cm}^{-3}$  in the cluster outskirts to above  $10^{-2} \text{ cm}^{-3}$  near the centre, is distributed such that the atmosphere is in hydrostatic equilibrium.

Coulomb interactions between electrons and ions in the ICM produces thermal bremsstrahlung (free-free) emission (Sarazin, 1988), with the majority of photons emitted in the X-ray band for typical cluster temperatures. At gas temperatures below  $3 \times 10^7$  K emission from metal recombination lines contributes significantly to the total luminosity (Peterson & Fabian, 2006). The total X-ray bolometric luminosity is given by  $L_X = \int n_e n_H \Lambda(T, Z) dV$ , where  $n_e$  and  $n_H$  are the electron and hydrogen densities and  $\Lambda(T, Z)$  is the cooling function, which reduces to  $\Lambda \propto T^{1/2}$  for pure bremsstrahlung emission. Gas densities are related to the overall normalization of the spectrum though the emission measure,  $\int n_e n_H dV$ , and gas temperature is determined mainly from the exponential cutoff in the spectral energy distribution.

Cluster surface brightness decreases rapidly with radius, and is well-described at intermediate radii by an isothermal  $\beta$ -model (Cavaliere & Fusco-Femiano, 1976):

$$I_X \propto [1 + (r/r_c)^2]^{-3\beta + \frac{1}{2}}, \quad (1.1)$$

where  $r_c$  is the core radius and  $\beta \approx 2/3$  is the ratio of the energy per unit mass in galaxies to that in the gas. For gas temperatures above 2 keV, surface brightness is nearly independent of temperature.

Relaxed clusters host cool cores (Hudson et al., 2010), so the isothermal approximation does not hold throughout the cluster. Following from hydrostatic equilibrium, the decreasing temperature toward the cluster nucleus is associated with a sharp increase in density (White et al., 1994). Since luminosity scales as the square of the electron density, the centers of cool core clusters are far brighter than a single  $\beta$ -model predicts. In the absence of heating this leads to a cooling flow, which is discussed further in the next section. The surface brightness profile of cool core clusters can be modelled more accurately by adding a second  $\beta$ -model to account for the lower temperature of the cluster core (e.g. Kirkpatrick et al. 2009).

## 1.2 Cooling Flows

The cool, dense cores of relaxed galaxy clusters are bright, and will radiate away their thermal energy in the cooling time,

$$t_{cool} = \frac{E_{thermal}}{L_X} = \frac{3}{2} \frac{p}{n_e n_H \Lambda(Z, T)}, \quad (1.2)$$

unless a source of heating compensates for radiative losses. Relaxed clusters have central cooling times that fall below 1 Gyr (Voigt & Fabian, 2004), dropping as low as a few  $10^8$  yr (Rafferty et al., 2008). These timescales are far shorter than either the age of the cluster or the time since the last major heating event, and lead to a cooling flow in the absence of another heating mechanism.

As the central gas loses energy to radiation it must be compressed in order to maintain hydrostatic equilibrium. It is then replenished by the overlying gas, resulting in a slow, steady inward flow of material that is known as a cooling flow (see Fabian 1994 for a review). Compression of the cooling gas increases its density, boosting the X-ray luminosity and increasing the rate of cooling. This results in a positive feedback loop in which unimpeded cooling causes the temperature of the hot atmosphere to drop catastrophically, rapidly falling below  $10^4$  K.

Cooling flows are expected to deposit mass out of the ICM at a rate of hundreds to thousands of solar masses per year, producing vast reservoirs of stars and molecular gas:

$$\dot{M} = \mu m_p \frac{2}{5} \frac{L_{cool}}{kT}. \quad (1.3)$$

Here  $L_{cool}$  is the X-ray luminosity within the cooling region,  $\mu \approx 0.61$  is the mean molecular weight of the plasma,  $m_p$  is the proton mass, and the factor of  $2/5$  arises from the enthalpy of a monatomic ideal gas. Gas cooling below 1 keV would produce several emission lines from the recombination of various charge states of iron L (Böhringer et al., 2002).

Observations of galaxy clusters have revealed a number of problems with the cooling flow model. Stars produced from the cooling gas would shine brightly at UV and optical wavelengths. Observations have detected star formation at rates of  $1 - 100 M_\odot \text{ yr}^{-1}$  (Johnstone et al., 1987; McNamara & O’Connell, 1989; O’Dea et al., 2004), falling several orders of magnitude below the rates predicted by the cooling flow model. Persistent cooling over several Gyr would produce  $\sim 10^{12} M_\odot$  of atomic and molecular gas distributed throughout the central 100 kpc. However, cool gas and star formation are generally observed in the central tens of kpc, and the reservoirs of molecular gas are far too small to account for the predicted cooling rates (Edge, 2001; Salomé & Combes, 2003).

High resolution spectroscopy from the *Chandra* and *XMM-Newton* X-ray Observatories has failed to detect spectral features of gas cooling below 1 keV. The apparent lack of gas cooling below 1/3 of the mean cluster temperature (Peterson et al., 2003; Peterson & Fabian, 2006) implies that the ICM is not cooling at the expected rates of  $100 - 1000 M_{\odot} \text{ yr}^{-1}$ . Instead, radiative losses are being offset by a source of heating. The most likely mechanism is heating from active galactic nuclei, which we discuss in detail in the following section.

### 1.3 Feedback from Active Galactic Nuclei

Solutions to the cooling flow problem require a source of heating that is finely tuned to the rate of cooling. X-ray luminosities in the range of  $10^{42} - 10^{44} \text{ erg s}^{-1}$  require a total energy of  $10^{60} - 10^{62} \text{ erg}$  injected within the central 100 kpc over the past 5 – 10 Gyr. If the heat is supplied at a fixed rate over the life of the cluster, then a slight excess in the rate of heating would lead to cooling times in excess of the Hubble time. Instead, a negative feedback loop, where the cooling ICM triggers a heating event that suppresses further cooling, is a more plausible way to reproduce the prevalence of cool cores in clusters. The most likely candidate is heating from active galactic nuclei (see McNamara & Nulsen 2007, 2012 for a review). In this model, accretion of the cooling gas onto the central black hole drives a relativistic jet that heats the ICM.

High resolution X-ray imaging has revealed disturbances in the ICM in the form of X-ray cavities and surface brightness edges. X-ray cavities are elliptical regions of decreased surface brightness that range in size from several to hundreds of kpc in diameter, and have been detected in over 70% of cool core clusters (Dunn et al., 2005; Dunn & Fabian, 2006; Fabian, 2012; Bîrzan et al., 2012). The surface brightness depressions correspond to bubbles that were inflated by a relativistic (radio) jet launched by the AGN. Radio synchrotron emission fills the cavities, originating from the relativistic electrons and magnetic field generated by the radio jet (Burbidge, 1956; Blandford & Rees, 1974; De Young, 2006). The jet also drives weak shocks in the ICM, which manifest as edges in X-ray surface brightness that encompass the cavities (e.g. Hydra A: Wise et al. 2007, Hercules A: Nulsen et al. 2005, and MS 0735.6+7421: McNamara et al. 2005).

#### 1.3.1 X-ray Cavities

During the early stages of an AGN outburst the jet advances supersonically through the ICM, carving out an elongated cavity that is overpressurized relative to the ICM (Blandford & Rees, 1974). As the jet slows the cavity expands rapidly, until it reaches pressure balance with its surroundings. The cavity disconnects from the jet when its buoyant velocity exceeds the expansion

velocity of the cavity (O’Dea, 1985), and proceeds to rise buoyantly through the ICM (Churazov et al., 2000, 2001). Observations show bright rims of cool gas surrounding many cavity systems, corresponding to displaced gas that is being dragged outward by the buoyantly rising bubbles (McNamara et al., 2000; Blanton et al., 2001).

Cavities are detected through the depression in surface brightness resulting from the absence of X-ray emitting gas (e.g. Bîrzan et al. 2004; Rafferty et al. 2006). As a result it is very difficult to detect small cavities – either from low power outbursts or cavities that are in their early stages of formation – which produce only a small deficit in the number of X-ray counts. It is easiest to detect large cavities located near the centres of clusters, where the X-ray luminosity is high (Bîrzan et al., 2012). Observations of cavities are therefore biased toward the largest outbursts, and the number of systems with observed cavities is likely an underestimate of the true fraction.

X-ray imaging provides a direct measure of the  $pV$  work required to inflate cavities. Additional energy is needed in order to displace the ICM, so the total cavity energy is given by its enthalpy:

$$E_{\text{cav}} = \frac{\gamma}{\gamma - 1} pV, \quad (1.4)$$

where  $p$  is the cavity’s pressure and  $V$  is its volume. Since cavities are in pressure balance with the surrounding gas, the pressure of a cavity can be estimated using the pressure of the ambient ICM (Begelman, 2004). The ratio of heat capacities,  $\gamma$ , is  $4/3$  for a relativistic gas and  $5/3$  for a non-relativistic, monatomic gas. Non-relativistic contents would be detectable unless its temperature exceeds 20 keV (McNamara & Nulsen, 2007). For relativistic contents the corresponding cavity enthalpy is  $E_{\text{cav}} = 4pV$ .

Cavity ages are estimated in three ways: the buoyant rise time, the sound crossing time, and the refill time (Bîrzan et al., 2004). A bubble rising at its terminal velocity,  $v_T \approx \sqrt{2gV/SC}$ , will reach its current position,  $R$ , in the buoyancy time (Churazov et al., 2001),

$$t_{\text{buoy}} = \frac{R}{v_T} = R \sqrt{\frac{SC}{2gV}}. \quad (1.5)$$

Here  $S$  is the cross-sectional area of the rising bubble,  $V$  is the bubble volume, and  $C \approx 0.75$  is the drag coefficient. The gravitational acceleration,  $g$ , can be determined under the assumption that the surrounding atmosphere is in hydrostatic equilibrium.

Assuming the bubble rises at the local sound speed,  $c_s = \sqrt{\gamma kT/\mu m_p}$ , its age is given by the sound crossing time,

$$t_{c_s} = \frac{R}{c_s} = R \sqrt{\frac{\mu m_p}{\gamma kT}}. \quad (1.6)$$

Finally, the refill time (McNamara et al., 2000) is the amount of time that it takes for the bubble to rise through its own diameter,

$$t_{\text{refill}} = 2\sqrt{\frac{r}{g}}, \quad (1.7)$$

where  $r$  is the radius of the cavity. This is indicative of the time it takes to refill the volume displaced by the cavity as the bubble rises. In general these timescales are consistent within a factor of  $\sim 2$ , with sound crossing time being the shortest, followed by the buoyancy time and then by refill time.

The mean power output by the AGN is simply the ratio of cavity enthalpy to its age,

$$P_{\text{cav}} = \frac{E_{\text{cav}}}{t_{\text{age}}} = \frac{4pV}{t_{\text{age}}}. \quad (1.8)$$

It is not entirely clear which timescale provides the best estimate of cavity age. Cavities located near the AGN are likely still dominated by the dynamics of the jet, in which case the sound crossing time is the natural choice. Toward larger radii buoyancy timescales are more representative of the cavity's true age. However, the cavity dynamics are initially driven by the jet, so it does not rise buoyantly for its whole life. Additionally, viscous (Reynolds et al., 2005) and magnetic (De Young, 2003) stresses may decrease the terminal speed. Furthermore, buoyancy times are calculated assuming a constant terminal velocity, which is not true. In general either the buoyancy time or the mean of the three timescales are used to estimate the cavity age. Outburst ages, which do not account for jet-driven dynamics, are likely overestimates of the true bubble age, resulting in an underestimate of cavity power.

Detailed studies of cavity systems have found that cavity enthalpies ranging from  $10^{56}$  erg in giant ellipticals to over  $10^{61}$  erg in rich clusters (Bîrzan et al., 2004; Rafferty et al., 2006). All of this energy can be thermalized as the bubble rises through the hot atmosphere (Churazov et al., 2002). Gravitational potential energy is converted to kinetic energy as gas replaces the void left by the rising cavity (Bîrzan et al., 2004), which is subsequently dissipated, heating the ICM. Cavity powers therefore represent the mean rate in which AGN inject energy back into the ICM, and range in value from  $10^{42}$  erg s $^{-1}$  in smaller systems to over  $10^{46}$  erg s $^{-1}$  in MS 0735.6+7421 (McNamara et al., 2005). Cavity power and X-ray bolometric luminosity are closely linked, with more than half of the systems containing outbursts powerful enough to completely offset radiative losses (Rafferty et al., 2006). Cavities inflated by AGN outbursts are therefore a convincing method for offsetting radiative losses and suppressing cooling flows.

### 1.3.2 Weak Shocks and Sound Waves

Weak shocks, driven by the initial supersonic advance of the jet, manifest as edges in X-ray surface brightness and are being revealed in a growing number of clusters (e.g. Hydra A: Nulsen et al. 2005, A2052: Blanton et al. 2011, MS 0735.6+7421: McNamara et al. 2005, and others). Surrounding the X-ray cavities, shock fronts encompass volumes that are 200-400 kpc in radius. With such large volumes, the energy required to drive the shock (David et al., 2001),

$$E_{\text{shock}} = \Delta p V, \quad (1.9)$$

exceeds  $10^{61}$  erg in many systems. In this equation  $\Delta p$  is the difference between post- and pre-shock pressures. Since AGN outbursts partition energy into driving a weak shock, cavity power provides only a lower limit on the total power output by the AGN.

Shock strength is determined from the magnitude of the surface brightness jump (e.g. Nulsen et al. 2005). Assuming a spherical shock from a point explosion, observed surface brightness jumps are best fit by Mach numbers of 1.2-1.7 (McNamara & Nulsen, 2007). From the Rankine-Hugoniot shock jump conditions, a Mach  $\mathcal{M}$  shock causes a temperature rise of

$$\frac{T_2}{T_1} = \frac{[(\gamma - 1)\mathcal{M}^2 + 2][2\gamma\mathcal{M}^2 - (\gamma - 1)]}{(\gamma + 1)^2\mathcal{M}^2}, \quad (1.10)$$

where  $T_2$  is the post-shock temperature,  $T_1$  is the pre-shock temperature, and  $\gamma = 5/3$  for the ICM. For a Mach 1.2 shock the corresponding temperature jump is 20%. In observations this jump is obscured by projection effects, reaching a peak of only  $\sim 5 - 10\%$ . As a result it is often difficult to detect the temperature rise caused by a shock front.

Since the shock speed is known, its age can be determined much more reliably than cavity ages. The time taken for a shock to travel to its current position is approximately  $t_{\text{shock}} = R/Mc_s$ , where  $c_s$  is the local sound speed. Typical shock ages are consistent with cavity rise times, which is reassuring given they originate from the same AGN outburst. The mean power required to drive the shock is therefore comparable to the cavity power, reaching  $10^{46}$  erg s<sup>-1</sup> in the most powerful systems (McNamara et al., 2005). Unlike cavities, however, a single shock contributes only a small fraction of its energy into heating the surrounding gas. Instead, repeated weak shocking is required in order to suppress cooling flows (Randall et al., 2011; Nulsen et al., 2013). Multiple generations of weak shocks have been detected in Perseus and M87, and possess ample energy to offset radiative losses. Additionally, weak shock heating decreases rapidly as a function of radius (McNamara & Nulsen, 2012), having the greatest effect near the nucleus, where it likely has an important role in maintaining the properties of the accreting gas.

Oscillating pressure disturbances have been found in bright, nearby systems undergoing AGN feedback, including Perseus (Fabian et al., 2006), A2052 (Blanton et al., 2011), and Centaurus

(Sanders & Fabian, 2008). The disturbances are caused by sound waves propagating through the cluster outskirts. Dissipation of sound waves is also able to heat the ICM, though this depends on uncertain transport coefficients (Fabian et al., 2005). In general shock heating dominates near the nucleus, sound waves heat the cluster outskirts, and cavities heat the gas at intermediate radii.

### 1.3.3 Powering AGN Outbursts

AGN outbursts are typically thought to be fuelled by accretion of the surrounding gas onto the central supermassive black hole. While most of the binding energy is transported into the black hole, a small fraction  $\epsilon$ , which is usually taken to be  $\sim 10\%$ , is converted into a momentum-driven jet. In order to fuel an outburst with energy  $E_{cav}$ , the mass that must be accreted is

$$M_{acc} = \frac{E_{cav}}{\epsilon c^2}. \quad (1.11)$$

For a  $10^{60} - 10^{62}$  erg outburst this corresponds to an accreted mass of  $\sim 5 \times 10^6 - 5 \times 10^8 M_\odot$ . This mass must originate from either the hot atmosphere or clumps of cold gas in the central galaxy.

Bondi accretion (Bondi, 1952) is the spherical accretion of the hot atmosphere onto the central black hole. It is sensitive to the central density ( $n_e$ ) and temperature ( $kT$ ) of the hot atmosphere as well as the mass of the black hole ( $M_{BH}$ ) through the relation

$$\frac{\dot{M}_B}{M_\odot \text{ yr}^{-1}} = 0.012 \left( \frac{n_e}{\text{cm}^{-3}} \right) \left( \frac{kT}{\text{keV}} \right)^{-3/2} \left( \frac{M_{BH}}{10^9 M_\odot} \right)^2. \quad (1.12)$$

Since  $n_e kT^{-3/2}$  is a power of the entropy index,  $K = n_e^{-2/3} kT$ , which responds directly to heating and cooling, the Bondi mechanism is simple to regulate. As the hot atmosphere radiates and cools, the Bondi accretion rate increases and triggers an AGN outburst. Heat from this outburst increases the entropy of the surrounding gas, decreasing the accretion rate and establishing a feedback loop. Though the central densities in giant ellipticals are large enough to support Bondi accretion, it is difficult to fuel outbursts greater than  $10^{45}$  erg  $\text{s}^{-1}$  via the accretion of the hot atmosphere (Rafferty et al., 2006; Hardcastle et al., 2007; McNamara et al., 2011). Additionally, even a small amount of angular momentum can decrease the Bondi accretion rate by several orders of magnitude (Proga & Begelman, 2003).

Gas cooling out of the hot atmosphere condenses into molecular clouds, which may then accrete onto the black hole. With molecular gas masses exceeding  $10^{10} M_\odot$  in many systems (Edge, 2001; Salomé & Combes, 2003), BCGs contain more than enough cold gas to fuel AGN

outbursts. Observations have revealed that this gas resides in a disk (e.g. Hydra A: Hamer et al. 2014; A1664: Russell et al. 2014), which allows for the regulation of the accretion rate. Nevertheless, it is difficult to understand how a disk a few kpc in radius is able to regulate cooling on scales of several hundred kpc. Furthermore, the low-density jet of an AGN outburst must couple to the molecular gas in order to subdue subsequent accretion. Recent ALMA observations of A1835 have indicated that this is the case, with  $10^{10} M_{\odot}$  of molecular gas displaced along the direction of the cavities (McNamara et al., 2014).

In the most powerful systems, like MS 0735.6+7421, an insufficient amount of either hot or cold gas surrounds the black hole, making fuelling the outburst through accretion alone difficult. Accessing the spin energy of a rapidly rotating black hole may ease the demands on accretion (Meier, 1999, 2001). McNamara et al. (2009) have shown that a maximally-spinning,  $10^9 M_{\odot}$  black hole contains  $\sim 10^{62}$  erg of spin energy, enough to power even the most energetic of outbursts. However, this mechanism still has a number of issues. Spinning up the black hole requires either the accretion of a substantial amount of gas or mergers with black holes of a comparable mass. Also, if the spin energy of the black hole is consumed in the outburst, then subsequent outbursts in the feedback cycle would again require the accretion of a substantial amount of surrounding gas.

### 1.3.4 Metal-Enriched Outflows

The centre of the intracluster medium is chemically enriched well in excess of the mean metallicity of approximately 1/3 solar, with central metallicities approaching solar (De Grandi & Molendi, 2001). This enrichment is likely caused by type Ia supernovae (De Grandi et al., 2004; Werner et al., 2008), but it extends to radii a few times larger than the stellar light (Rebusco et al., 2005, 2006; David & Nulsen, 2008). Detailed metal maps of the ICM have shown that metal-rich regions are preferentially aligned with the direction of radio jets (Kirkpatrick et al., 2009; Simionescu et al., 2009; Gitti et al., 2011), implying that AGN outbursts are able to couple to the metal-rich gas and displace it toward higher altitudes. The maximum radius of the uplifted material, the “iron radius”, is related to the total power of the jet through the scaling relation  $R_{\text{Fe}} \propto P_{\text{jet}}^{0.45}$  (Kirkpatrick & McNamara, in preparation).

These metal outflows are uplifting huge amounts of gas. Typical masses of iron alone range from  $\sim 10^5 - 10^8 M_{\odot}$ , translating to a total uplifted mass of  $10^8 - 10^{11} M_{\odot}$  with a mean of  $\sim 10^{10} M_{\odot}$  (Kirkpatrick & McNamara, in prep). For an outburst age of  $10^8$  yr, this implies an average outflow rate of  $\sim 100 M_{\odot} \text{ yr}^{-1}$ . Entrainment of central gas in the radio jet therefore has a significant impact on cooling flows, which are expected to cool gas at similar rates. Uplifted gas falling back toward the nucleus can also heat the ICM, though this effect can only balance 10 –

20% of the rate of cooling. Furthermore, removing the supply of cool, central gas can potentially quench accretion (McCarthy et al., 2008), playing a critical role in the feedback process by halting the AGN outburst.

### 1.3.5 Repeated Outbursts

Cooling persists over the lifetime of clusters, so multiple heating events are required to suppress cooling in the long term. As soon as an AGN outburst terminates, or simply stops heating the central gas, a cooling flow will reestablish itself on a timescale comparable to the central cooling time. AGN must therefore rejuvenate on timescales shorter than the central cooling time in order to prevent catastrophic cooling (Dunn & Fabian, 2006; Rafferty et al., 2008; Bîrzan et al., 2012). Clusters with strong cool cores have central cooling times as short as a few  $10^8$  yr (Rafferty et al., 2008; Hudson et al., 2010), implying that AGN must rejuvenate on timescales of  $\sim 10^8$  yr.

Deep Chandra observations of cool core cluster have begun to reveal multiple generations of X-ray cavities. A striking example of this is Hydra A (Wise et al., 2007), where three generations of cavities are clearly visible on either side of the nucleus and rejuvenate every  $\sim 1.5 \times 10^8$  yr, which is slightly shorter than the  $2 \times 10^8$  yr central cooling time. Multiple generations of cavities have currently been detected in 10 systems: Perseus (Fabian et al., 2006), M87 (Forman et al., 2007), Hydra A (Wise et al., 2007), HCG 62 (Rafferty et al., 2013), Abell 2199 (Nulsen et al., 2013), Abell 2052 (Blanton et al., 2009, 2011), NGC 5813 (Randall et al., 2011), Abell 3581 (Canning et al., 2013), NGC 5846 (Machacek et al., 2011), and MS 0735.6+7421 (Vantghem et al., 2014).

AGN rejuvenation can either be a continuous process or can occur after a period of quiescence. Bîrzan et al. (2012) found that cavities are present in over 70% of cool core clusters in the Brightest 55 clusters of galaxies (B55; Edge et al. 1990) and Highest X-ray FLUX Galaxy Cluster Sample (HIFLUGCS; Reiprich & Böhringer 2002), though undetected cavities may push this number closer to 100%. The high duty cycle for AGN feedback implies that AGN are active for most of duration of the cooling flow, but may not be “on” continuously. The mean power output by the AGN in systems with multiple generations of cavities varies by factors of a few to several tens. Consecutive outbursts would then be consistent with bubbles detaching from the radio jet as the power falls below a certain threshold. Finally, the morphologies of several radio galaxies suggest that sequential AGN outbursts are triggered after a period of quiescence (Schoenmakers et al., 2000; Saripalli et al., 2002).

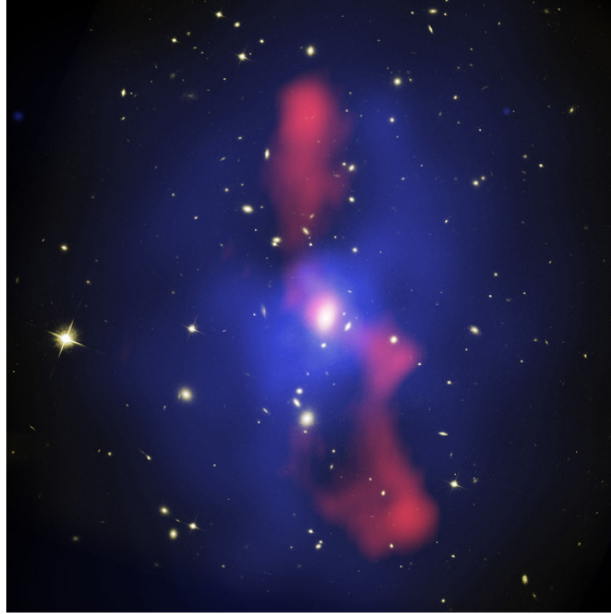


Figure 1.1: Composite Chandra X-ray (blue), VLA radio (red), and HST optical (yellow) image of the galaxy cluster MS 0735.6+7421. Credit: McNamara et al. (2009).

## 1.4 MS 0735.6+7421

The cool core cluster MS 0735.6+7421 (hereafter MS0735), shown in Figure 1.1, hosts unusually large X-ray cavities in an otherwise relaxed atmosphere (Gitti et al., 2007). Each cavity has a diameter of roughly 200 kpc and is filled with synchrotron emission from the radio jet. A weak but powerful shock front encompasses the cavities (McNamara et al., 2005). The total energy required to inflate the bubbles and drive the shock front exceeds  $10^{62}$  erg, making this the most energetic AGN outburst known. The mechanical power output of MS0735, in excess of  $10^{46}$  erg  $s^{-1}$ , rivals the radiative power of a quasar.

The powerful outburst in MS0735 challenges our understanding of how galaxies and supermassive black holes coevolve and how AGN are powered. Powering a  $10^{62}$  erg AGN outburst over  $\sim 10^8$  yr requires the accretion of  $5 \times 10^8 M_{\odot}$  of gas at a mean rate of  $3 - 5 M_{\odot} \text{ yr}^{-1}$ . At the same time, far UV imaging has revealed no trace of star formation or emission from a nuclear point source (McNamara et al., 2009). Containing less than  $3 \times 10^9 M_{\odot}$  of cold molecular gas (Salomé & Combes, 2008), an implausibly large fraction of MS0735's molecular gas supply must be accreted in order to power this outburst.

Bondi accretion also has difficulty powering this outburst. McNamara et al. (2009) report a

black hole mass of  $5 \times 10^9 M_\odot$  using their V-band luminosity of  $M_V = -23.91$  and the scaling relations of Lauer et al. (2007). The gas density ( $n_e \approx 0.13 \text{ cm}^{-3}$ ) and temperature ( $kT \approx 2.5 \text{ keV}$ ) within the central 3.5 kpc translate to a Bondi accretion rate of  $5 \times 10^{-3} M_\odot \text{ yr}^{-1}$ , far below the  $3 - 5 M_\odot \text{ yr}^{-1}$  required to power the outburst. Although gas entropy continues to decrease toward the nucleus (Panagoulia et al., 2014), the increase in density required to achieve an adequate Bondi rate would produce a spike in luminosity that would be detectable in X-ray images. Instead, if Bondi accretion is to be feasible, MS0735 must host an ultramassive black hole with mass approaching  $10^{11} M_\odot$ . McNamara et al. (2009) argue that the large stellar core in MS0735’s BCG may well be indicative of a black hole with mass  $7 \times 10^{10} M_\odot$ , though it is not clear if the relations of Kormendy & Bender (2009) extend to such high masses. Alternatively, a maximally-spinning,  $5 \times 10^9 M_\odot$  black hole contains ample rotational energy to power this outburst (McNamara et al., 2009, 2011). Tapping black hole spin would ease the demands on accretion, although this suggestion presents a number of additional problems, as outlined in Section 1.3.3.

This thesis seeks to investigate the impact of a powerful radio jet on its surroundings. To this effect, we present an analysis of a deep (450 ks) Chandra X-ray observation of MS 0735.6+7421. This observation allows us to trace the interaction between radio jet and the intracluster medium by studying the cavities, weak shock front, and gas entrainment. Results from this analysis have recently been published in Vantyghem et al. (2014). We also use integral field spectroscopy from the Gemini observatory to map the  $H\alpha$  nebula in the BCG.

This thesis is organized as follows: We outline the observations and data reduction in Chapter 2. Cluster profiles and maps derived from the X-ray properties are presented in Chapter 3. In Chapter 4 we present updated measurements of cavity and shock energetics and outline how the large outburst in MS0735 affects the ICM. Evidence for a rejuvenated AGN outburst is presented in Chapter 5. In Chapter 6 we present the first comparison of outburst interval to central cooling time and cavity heating time for the 11 objects that have two generations of AGN outbursts. We present preliminary results from an analysis of Gemini integral field spectroscopy in Chapter 7. Finally, the results are summarized in Chapter 8.

All errors are quoted at the  $1\sigma$  level unless otherwise stated. A standard  $\Lambda$ CDM cosmology is assumed, with  $H_0 = 70 \text{ km s}^{-1} \text{ Mpc}^{-1}$ ,  $\Omega_m = 0.3$ , and  $\Omega_\Lambda = 0.7$ . MS0735 lies at a redshift of 0.216 (Stocke et al., 1991), corresponding to a luminosity distance of 1070 Mpc and an angular scale of  $1 \text{ arcsec} = 3.5 \text{ kpc}$ .

## Chapter 2

# Observations and Data Reduction

This analysis combines seven *Chandra* observations of MS0735.6+7421 taken on the ACIS-I detector in June 2009. The cumulative exposure time for these observations is 477 ks. Table 2.1 summarizes the exposure times for each observation. Each observation was reprocessed with CIAO version 4.5 and CALDB version 4.5.6, which were provided by the *Chandra* X-ray Center. The level 1 event files were reprocessed to apply the latest gain and charge transfer inefficiency correction and then filtered to remove photons detected with bad grades. The additional data obtained in VFAINT mode were used to improve screening of the particle background. Background light curves were extracted from the level 2 events files of chip 0 on the ACIS-I detector. These background light curves were filtered using the LC\_CLEAN script provided by M. Markevitch in order to identify periods affected by flares. None of the observations showed any significant flares. The final cleaned exposure time was 447 ks.

The cleaned events files were then reprojected to match the position of the observation with obs ID 10468. An image for each observation was produced by summing events in the energy range 0.5 – 7.0 keV. These images were then summed to create a single image for identifying features in the X-ray emission. Point sources were identified using WAVDETECT (Freeman et al., 2002). The identified point sources were inspected visually and excluded from subsequent analysis. The final image, with point sources removed, is shown in Figure 2.1. The image is not corrected for exposure.

Blank-sky backgrounds were extracted for each observation, processed the same way as the events files, and reprojected to the corresponding position on the sky. Each blank-sky background was normalized to the 9.5 – 12 keV energy band in the observed data set. This was a 10 – 15% correction for all observations. The normalized blank-sky background data sets were compared to source-free regions of the observed data set for consistency, and were found to be a close

Table 2.1: Exposure Times.

| Obs ID | Date          | Exposure Time<br>(ks) | Cleaned<br>Exposure Time (ks) |
|--------|---------------|-----------------------|-------------------------------|
| 10468  | June 21, 2009 | 46.0                  | 41.7                          |
| 10469  | June 11, 2009 | 93.3                  | 86.7                          |
| 10470  | June 16, 2009 | 142                   | 134.8                         |
| 10471  | June 25, 2009 | 19.5                  | 18.1                          |
| 10822  | June 18, 2009 | 75.4                  | 71.8                          |
| 10918  | June 13, 2009 | 65.2                  | 61.8                          |
| 10922  | June 26, 2009 | 35.4                  | 32.3                          |
| Total  |               | 477                   | 447                           |

match to the background of the observed data set.

Spectral data were analyzed by first extracting source spectra and background spectra from each observation independently. All extracted spectra and background spectra were summed and the exposure times were adjusted accordingly. Spectra may be summed because each observation was taken on the same detector over the course of about 2 weeks. The roll angles are similar, so spectral extraction regions are from similar regions of the chip and therefore have similar responses. Auxiliary response files were weighted by the number of counts in the spectrum and summed using the `ADDARF` command. The redistribution matrix files were also weighted by the number of counts and summed using `ADDRMF`. Finally, the summed spectrum was binned to a minimum of 20 counts per energy bin.

The loss of area resulting from point sources and chip gaps was corrected by creating an exposure map for each observation with the `MKEXPMAP` command in `CIAO`, omitting effective area and quantum efficiency. Each exposure map was weighted by exposure time, summed, and then normalized by the total exposure time. The appropriate area correction was obtained from the mean value of this exposure map within the region of interest. The correction was applied to the spectrum and background spectrum by setting the `AREASCAL` keyword.

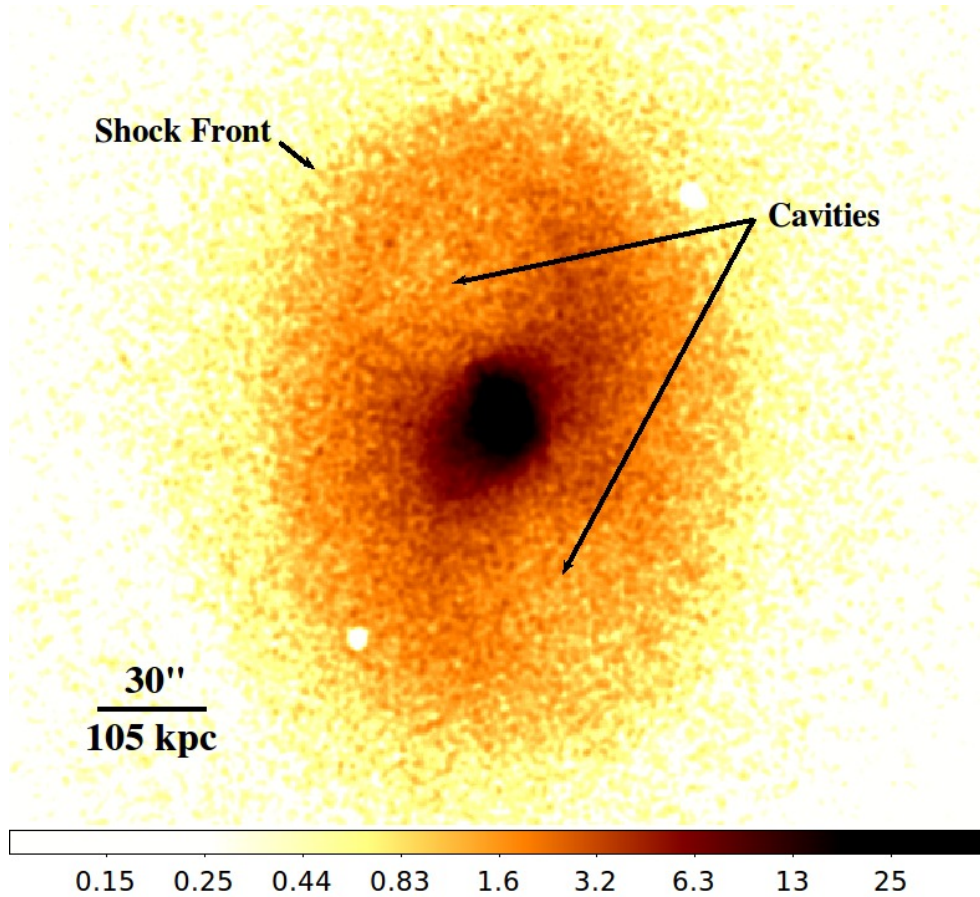


Figure 2.1: *Chandra* X-ray image (0.5 – 7 keV) of MS 0735.6+7421 in units of counts pixel<sup>-1</sup> and Gaussian-smoothed with a 3 pixel (1.5'') kernel radius. In this image North is up and East is to the left. Two cavities and a shock front are visible. Point sources have been excluded from the image.

# Chapter 3

## Cluster X-ray Properties

We begin our X-ray analysis of MS0735 by identifying morphological features in the intracluster medium. These include two cavities exceeding 200 kpc in diameter encompassed by a cocoon shock in an otherwise relaxed atmosphere. Next we quantify gas temperature, electron density, and metal abundance, along with their derived quantities using projected radial profiles. A detailed deprojection analysis is then employed in Section 3.3 to produce radial profiles that better describe the cluster centre. In Section 3.4 we present two-dimensional maps of temperature and abundance, comparing local variations in these maps to the morphological features from Section 3.1 and the profiles in Section 3.2. Multiphase gas is detected in the cluster centre, and is described in Section 3.5. Finally, in Section 3.6 we quantify the X-ray luminosity that must be offset by heating in order to suppress a cooling flow.

### 3.1 Surface Brightness

Cluster surface brightness was extracted from the X-ray image for a series of concentric elliptical annuli. The annuli had a spacing of  $1''$  (3.5 kpc) along the minor axis and were concentric with the shock front. The resulting surface brightness profile, after background subtraction, is shown in Figure 3.1. An isothermal, single- $\beta$  model (Equation 1.1) is a poor fit to this profile. Instead, we fit the surface brightness profile with a double- $\beta$  model to account for the excess emission from the cool core of the cluster. The core was best fit by a  $\beta$ -model with a normalization of 200 counts/arcsec<sup>2</sup>, a scale radius of 50 kpc, and a  $\beta$  of 1.8. The normalization of the second component was 20 counts/arcsec<sup>2</sup>, with  $r_{c_2} = 200$  kpc and  $\beta_2 = 0.9$ . The double- $\beta$  model is a poor fit beyond  $\sim 200$  kpc because of the shock front at 245 kpc, but is a reasonable fit in the cluster centre.

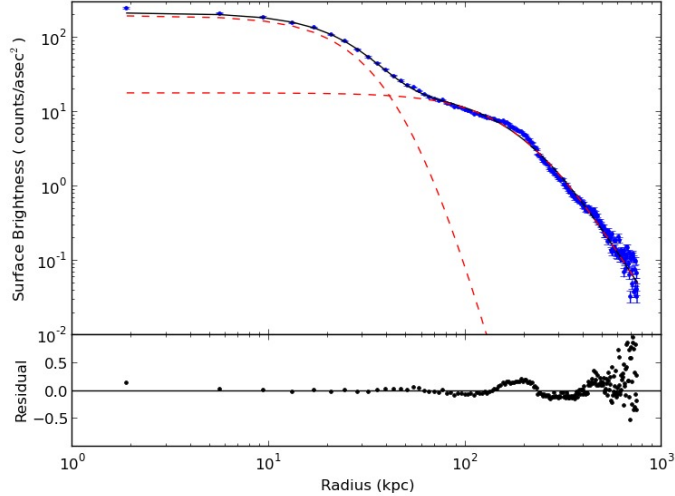


Figure 3.1: Elliptical surface brightness profile fit by a double- $\beta$  model. The blue points show the observed surface brightness profile, while the solid black line is the best fit obtained from the double- $\beta$  model. The dashed red lines show the individual components of the double- $\beta$  model. The residuals are normalized by model values and are shown in the bottom panel.

Subtracting the best-fitting double- $\beta$  model from the cluster emission produces the image shown in Figure 3.2. Two large cavities are easily visible in this image. Sharp edges surround the northeastern (NE) cavity, causing it to be more well-defined than the southwestern (SW) cavity. Bright emission is observed extending northwest and southeast from the nucleus. This likely corresponds to gas that has been displaced by the cavities, which were initially launched toward the northeast and southwest, but then rose buoyantly toward the north and south, respectively, pushing aside the ICM as they rose. The knot of bright emission  $\sim 20''$  east of the centre corresponds to cool, extended emission. The cocoon shock enveloping the cavities is also evident in Figure 3.2. The large positive residual between  $\sim 150 - 250$  kpc is located along the inner edge of the shock front (245 kpc) and is caused by gas that has presumably been displaced by the cavities.

### 3.2 Projected Profiles

Radial profiles of temperature, density, and abundance were created by fitting spectra extracted from elliptical annuli. Each elliptical annulus was taken to have the same major-to-minor axis

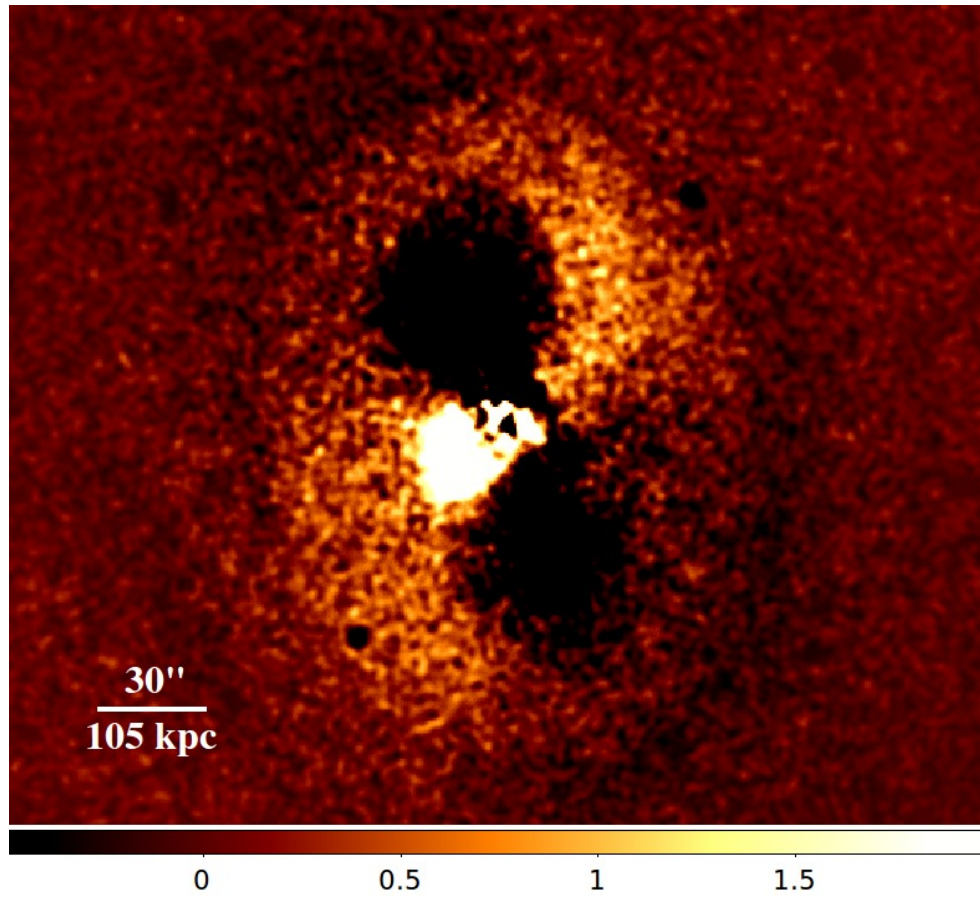


Figure 3.2: Residual image after subtracting a double- $\beta$  model from the X-ray image. The image is in units of counts  $\text{pixel}^{-1}$  and is Gaussian-smoothed with a  $2''$  kernel radius. The dark regions to the NE and SW correspond to the two large cavities in MS0735. A surface brightness edge surrounds these cavities and corresponds to a weak shock front.

ratio (1.37) and position angle ( $7^\circ$  east of north) as the outer shock front, which was determined by eye. The volume of each annulus was calculated assuming prolate symmetry. The inner 6 annuli were created with a fixed radial bin width of 7 kpc along the minor axis, which was chosen based on the  $1''$  spatial resolution of *Chandra*. These regions contained between 4000 and 10000 net counts. The remaining annuli were created with the number of counts increasing with radius, with the outermost annulus containing  $\sim 30000$  net counts. Projected temperature, density, pressure, abundance, cooling time, and entropy profiles are shown in Figure 3.3 and are plotted against the semi-minor axis of the annulus.

### 3.2.1 Spectral Fitting

Projected gas properties were determined by fitting each extracted spectrum with an absorbed single-temperature PHABS(MEKAL) model (Mewe et al., 1985, 1986; Balucinska-Church & McCammon, 1992; Liedahl et al., 1995) in XSPEC 12 (Arnaud, 1996). Temperature, normalization, and abundance were allowed to vary while the foreground column density,  $N_H$ , was fixed to the Galactic value of  $3.1 \times 10^{20}$  atoms  $\text{cm}^{-2}$  (Kalberla et al., 2005; Hartmann & Burton, 1997). This value is consistent with fitted values in the outskirts of the cluster within  $1\sigma$ . Abundance line ratios were set to the values given in Anders & Grevesse (1989) for consistency with previous work.

Density is related to the normalization of the MEKAL thermal model through the emission integral  $\int n_e n_H dV$ . The electron and hydrogen densities,  $n_e$  and  $n_H$ , are taken to be constant within each annulus. All emission in an annulus is assumed to originate from a prolate ellipsoid. Assuming hydrogen and helium mass fractions of  $X = 0.75$  and  $Y = 0.24$  (Anders & Grevesse, 1989) gives  $n_e = 1.2 n_H$ . Density can then be determined from the normalization of the thermal model and the volume of the ellipsoid. Pressure is determined from temperature and density using the ideal gas law,  $P = 2n_e kT$ .

### 3.2.2 Temperature Profile

The observed temperature profile, shown in the upper left panel of Figure 3.3, is consistent with the profiles from Vikhlinin et al. (2005). The mean projected temperature within 10 kpc of the cluster centre is  $3.23 \pm 0.11$  keV. It rises to a maximum of  $7.2 \pm 0.3$  keV at 220 kpc, where it drops abruptly to  $6.4 \pm 0.2$  keV. The temperature beyond this radius is roughly constant at  $\sim 6.1$  keV. The sharp drop in temperature at 220 kpc is interpreted as a weak shock front (see McNamara et al. 2005). The ratio between post- and preshock temperatures,  $1.13 \pm 0.06$ , is consistent with the projected temperature jump of  $\sim 10\%$  expected from the shock measurement.

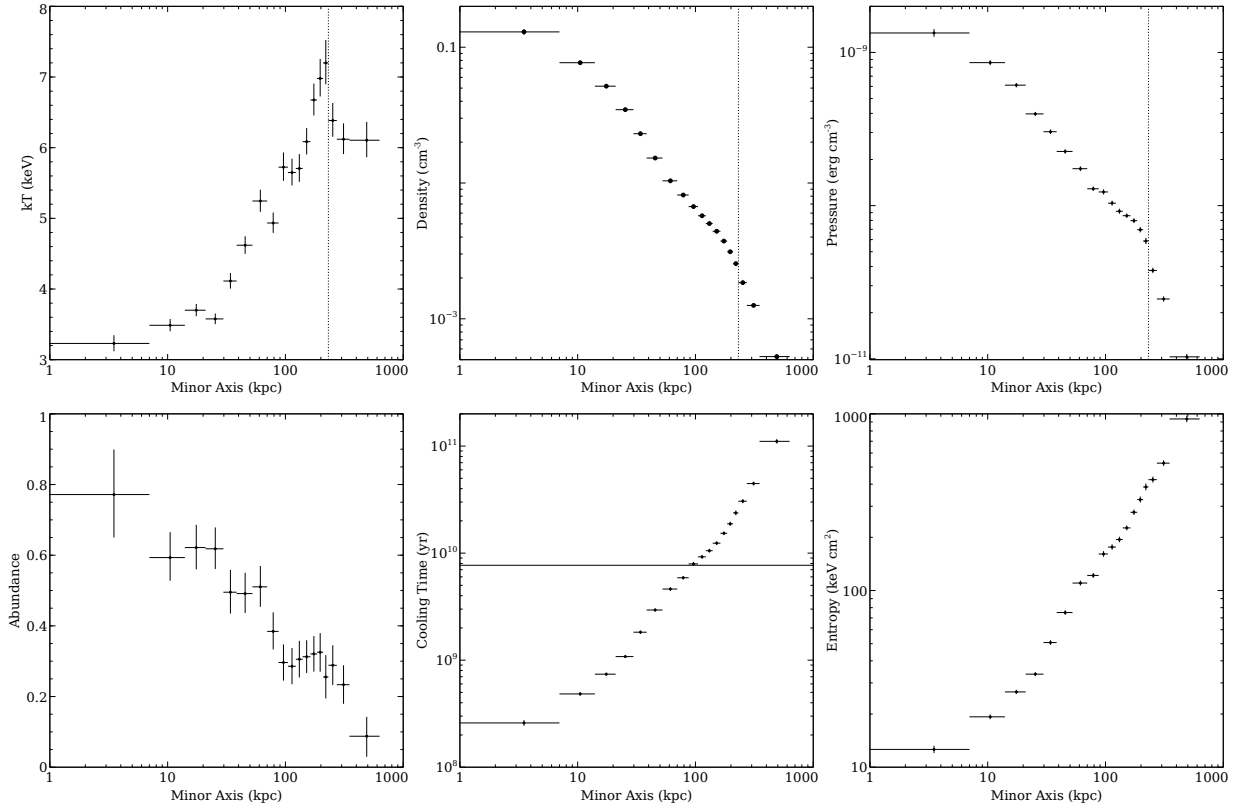


Figure 3.3: Projected temperature, density, pressure, abundance, cooling time, and entropy profiles. The profiles were created using elliptical annuli that are concentric with the outer shock front. All values are plotted against the semi-minor axis of the elliptical annulus. The dotted line in the temperature, density, and pressure profiles shows the approximate location of the outer shock front. Projected measurements overestimate the central density by up to a factor of 2 within  $\sim 30$  kpc, but are accurate toward larger radii. Refer to the deprojected profiles in Figure 3.4 for accurate central densities.

This shock, with a Mach number 1.26 determined from the surface brightness profile, is discussed further in Section 4.3.

The decrease in temperature at 25 kpc corresponds to cool gas that extends to the south-east, which coincides with the bright residual from Figure 3.2. This feature is evident in the temperature map discussed in Section 3.4. Significant scatter about the mean temperature is observed at  $\sim 80$  kpc, resulting from excess emission that extends perpendicular to the jet axis. This emission is visible in Figure 3.2, and may correspond to gas that has been displaced by the cavities.

### 3.2.3 Abundance Profile

The metal abundance within 10 kpc of the cluster centre is  $0.77 \pm 0.12 Z_{\odot}$ , and then decreases with radius. The abundance rise toward the cluster centre is likely due to enrichment from supernovae in the BCG (de Grandi & Molendi, 2009). From  $\sim 100 - 300$  kpc the abundance flattens to  $0.3 Z_{\odot}$ , which is typical of cool core clusters (De Grandi & Molendi, 2001; De Grandi et al., 2004). The last radial bin has an abundance of  $Z = 0.09_{-0.05}^{+0.06} Z_{\odot}$ ,  $3\sigma$  below the  $0.3 Z_{\odot}$  plateau.

### 3.2.4 Entropy Profile

The entropy index of intracluster gas, defined as  $K = kT n_e^{-2/3}$ , offers a more direct insight into heating and cooling processes than either temperature or density individually. Above  $\sim 20$  kpc the entropy index can be fit by a powerlaw with slope 1.07, which is consistent with the slopes found by Voit & Donahue (2005). Toward the centre the mean entropy index appears to flatten toward the central projected value of  $12.6 \pm 0.6$  keV cm<sup>2</sup>. Projection effects cause the central entropy to be underestimated, leading to a stronger entropy core.

### 3.2.5 Cooling Time

If uncompensated by heating the ICM will radiate away its thermal energy on a timescale  $t_{cool} = 3p / [2n_e n_H \Lambda(Z, T)]$ , where  $\Lambda(Z, T)$  is the cooling function as a function of metallicity,  $Z$ , and temperature,  $T$ . The cooling function is determined from the X-ray bolometric luminosity, which is given by  $L_X = \int n_e n_H \Lambda(Z, T) dV$  and is obtained by integrating the unabsorbed thermal model between 0.1 and 100 keV. The cooling time in MS0735, shown in Figure 3.3, roughly follows a powerlaw with a slope of 1.4. The projected cooling time within the central 10 kpc is  $(2.6 \pm 0.2) \times 10^8$  yr. Projection effects have a significant effect on central density, and therefore on central cooling time. The deprojected profile is presented in Section 3.3.

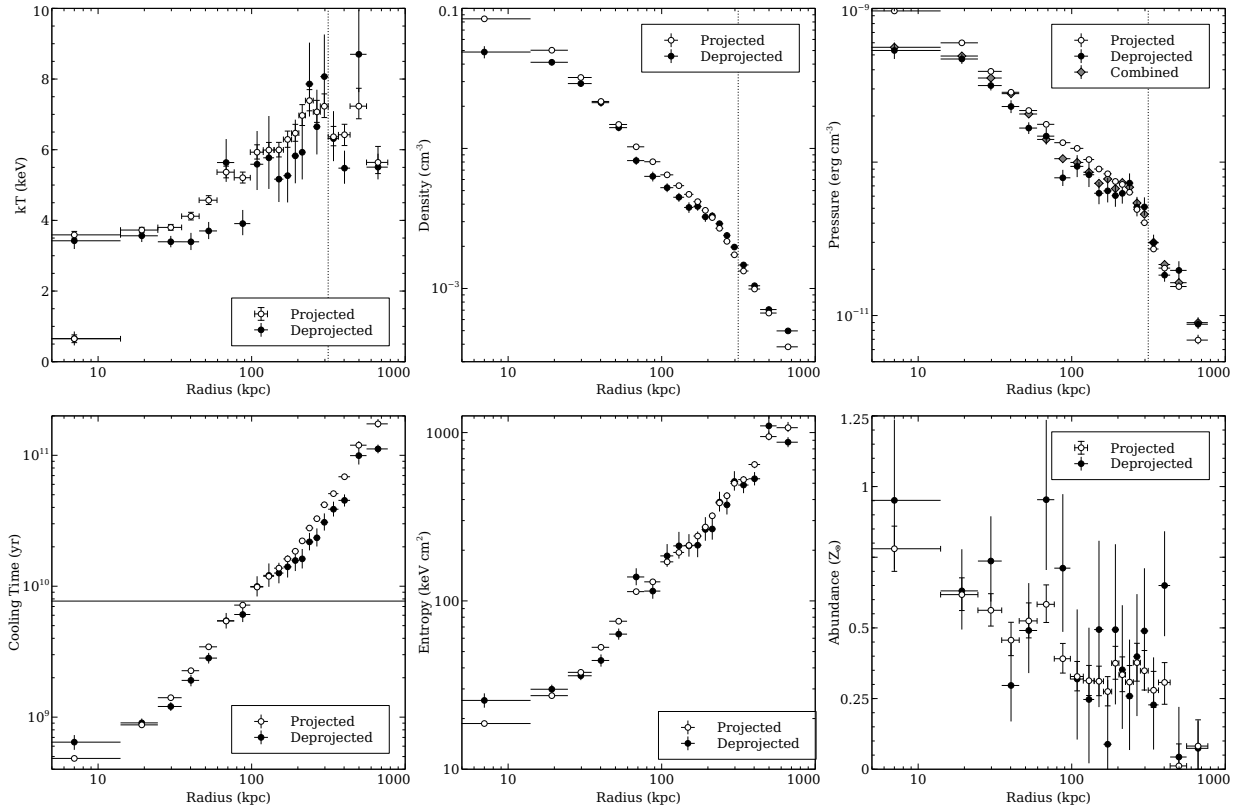


Figure 3.4: Projected (open circles) and deprojected (filled circles) profiles of temperature, density, pressure, cooling time, entropy, and abundance. The dotted line shows the location of the temperature jump, which is consistent with the location of the shock. Deprojection was performed using the model-independent DSDEPROJ. Including a second temperature component in the central region was found to improve the fit. The grey diamonds in the pressure profile correspond to pressure values calculated using deprojected densities and projected temperatures.

### 3.3 Deprojected Profiles

Projected foreground and background emission skews central projected densities and temperatures to higher values. We now correct for this effect by employing deprojected fits to radial profiles. Spectra were extracted from concentric circular annuli containing roughly 13000 net counts per annulus. These spectra were area-corrected, then deprojected using the model-independent DSDEPROJ package described in Sanders & Fabian (2007) and Russell et al. (2008). The absorbed thermal model described in Section 3.2.1 was fit to each of the deprojected spectra, and the resulting profiles are shown in Figure 3.4. The “onion-peeling” approach of the PROJCT model produces fits that are consistent with DSDEPROJ. Projected profiles were created using these regions and are plotted alongside the deprojected profiles for comparison. Two data points are plotted in the central bin due to the presence of multiphase gas, which is discussed in detail in Section 3.5.

Deprojection subtracts the line-of-sight contribution of overlying gas from each annulus. The presence of the X-ray cavities results in a decrease in density at  $\sim 100$  kpc. Gas displaced by the cavities, however, has an opposite effect on the density of an annulus, so masking out the cavities would result in an artificially increased density at intermediate radii. We therefore do not exclude the cavities from our deprojection. However, we note that the line-of-sight contribution to the central densities may be underestimated, though we expect this effect to be small. At the centre of the cluster the deprojected density is  $(4.9 \pm 0.5) \times 10^{-2} \text{ cm}^{-3}$ , which is significantly smaller than the central projected density of  $(8.4 \pm 0.2) \times 10^{-2} \text{ cm}^{-3}$ . The deprojected central temperature, on the other hand, is consistent with the projected temperature within  $1\sigma$ . The temperature of the cold phase in the central region is consistent between projected and deprojected profiles.

The projected temperature profile increases smoothly between 20 and 100 kpc, while the deprojected profile varies significantly. The deprojection relies critically on the assumption of spherical symmetry, which clearly fails here and contributes to the bouncing deprojected temperatures. The drop in projected temperature seen at this location in Figure 3.3 is exaggerated by the deprojection. The pressure profile used for subsequent calculations of cavity and shock properties combines deprojected densities with projected temperature in order to avoid the unstable solutions in the deprojected temperature profile.

At a radius of 315 kpc the projected temperature jumps from a preshock value of  $6.4 \pm 0.3$  keV to a postshock value of  $7.2 \pm 0.3$  keV. This temperature jump,  $1.14 \pm 0.07$ , is consistent with the jump observed in Figure 3.3. The deprojected profile shows a larger jump,  $1.3 \pm 0.2$ , but it is consistent with the projected jump within  $1\sigma$ . The location of this jump is consistent with the location of the shock front, which extends from 245 kpc along its minor axis to 335 kpc along its major axis.

The lower central density obtained through deprojection corresponds to an increase in central entropy, reaching a value of  $26 \pm 3 \text{ keV cm}^2$  in the central 14 kpc. This measurement is consistent with previous work (McNamara et al., 2005; Gitti et al., 2007), and arises from the heating of the central gas by the AGN (Voit & Donahue, 2005). However, Panagoulia et al. (2014) have shown that entropy cores are an artifact of resolution, and should continue to decrease toward the nucleus. The presence of multiphase gas in the central region is consistent with this result. With a central density and temperature of  $0.244 \text{ cm}^{-3}$  and  $0.65 \text{ keV}$ , respectively (see Section 3.5), the entropy index of the cold gas component,  $2 \text{ keV cm}^2$ , is consistent with a fraction of the gas continuing to cool to low temperatures.

## 3.4 Maps

Local variations in cluster abundance and temperature are traced using maps created with the CONTBIN<sup>1</sup> method (Sanders, 2006). Cluster emission is grouped into bins that closely follow surface brightness. The minimum signal-to-noise was set to 60 (3600 net counts) for the temperature map in order to produce an image with high spatial resolution. Accurate abundance measurements require more counts, so a signal-to-noise of 80 (6400 net counts) was used for this map. A spectrum was extracted from each region produced by CONTBIN and was fit with the absorbed thermal model described in Section 3.2.1. The maps are shown in Figure 3.5 and are both in broad agreement with the profiles in Figure 3.3. Point sources have been excluded from these maps.

### 3.4.1 Temperature Map

The approximate location of the outer shock front is indicated by the black ellipse overlaid on the temperature map (Figure 3.5, left). A clear temperature jump is seen between the pre- and post-shock bins along the entire shock front. The ratio of postshock to preshock temperature varies between 1.15 and 1.3 along the shock front. Accounting for projection effects, these jumps slightly exceed expected jump for the Mach 1.26 shock reported in this work. See Section 4.3 for a more detailed analysis.

An extended region of cooler emission is seen to the immediate SE of the cluster core, coinciding with the bright emission seen in Figure 2.1 (right). The temperature of this gas,  $4.5 \pm 0.2 \text{ keV}$ , is cooler than the surrounding  $\sim 5.5 \text{ keV}$  gas. The drop in temperature observed in Figure 3.3 is consistent with the location of this extended feature.

---

<sup>1</sup><http://www-xray.ast.cam.ac.uk/papers/contbin>

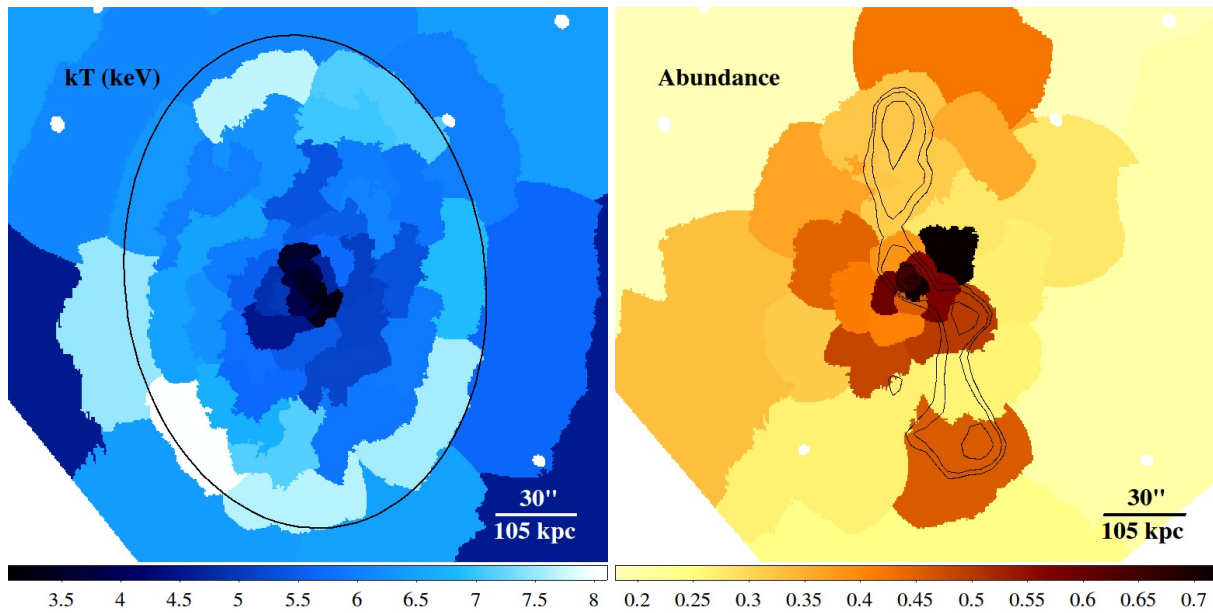


Figure 3.5: Temperature (left) and abundance (right) maps created by grouping regions of similar surface brightness. The colourbars give the temperature and abundance in units of keV and  $Z_{\odot}$ , respectively. Typical errors are 5% for temperature and 15 – 20% for abundance. Point sources have been excluded from the images. The black ellipse in the temperature map outlines the qualitative fit to the shock front as determined from the 0.5 – 7.0 keV X-ray image. A temperature jump is visible across the shock front. 327 MHz radio contours are overlaid on the abundance map.

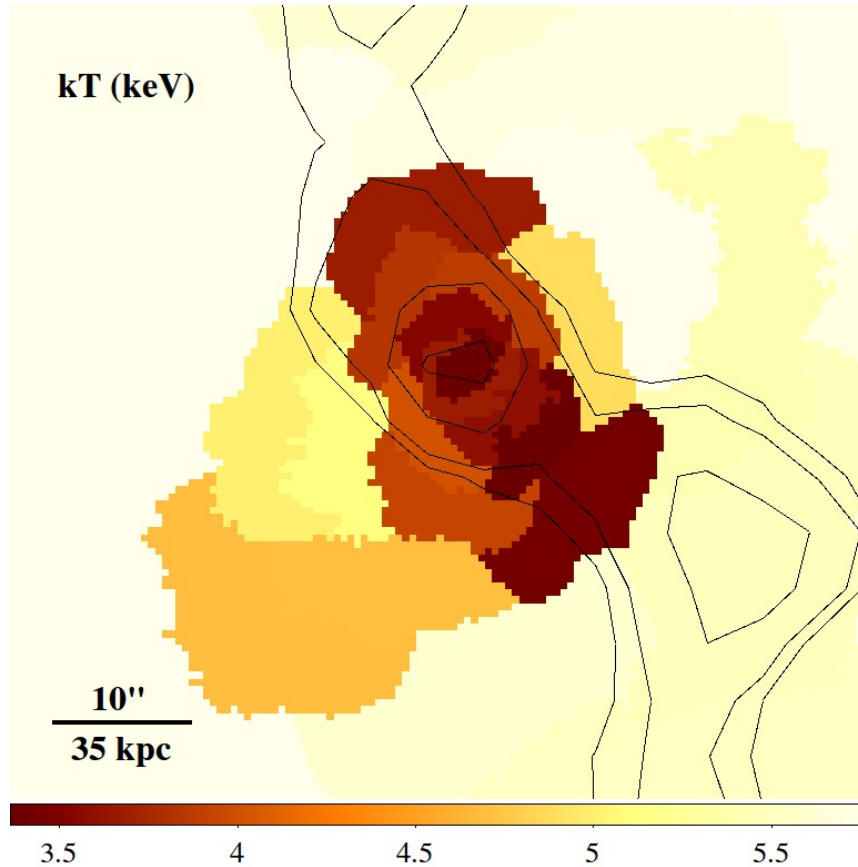


Figure 3.6: Inner 200 kpc of the temperature map presented in Figure 3.5. Low temperature gas from the centre of the cluster is entrained in the radio jet (black contours).

The central  $\sim 200$  kpc of the temperature map is shown in Figure 3.6 and is overlaid with 327 MHz VLA radio contours (Birzan et al., 2008). Cooler gas ( $\sim 3.5$  keV), which likely originates from the centre of the cluster, extends along the direction of the radio jets, implying that the ICM is entrained in the radio jet and is being dragged to high altitudes. This effect has also been observed in Hydra A, where the energy required to uplift the cool gas is comparable to the work required to inflate the cavities (Gitti et al., 2011). Removing the supply of low entropy gas near the cluster centre slows the rate of cooling, which is an important step in regulating AGN feedback (Kirkpatrick et al., 2009).

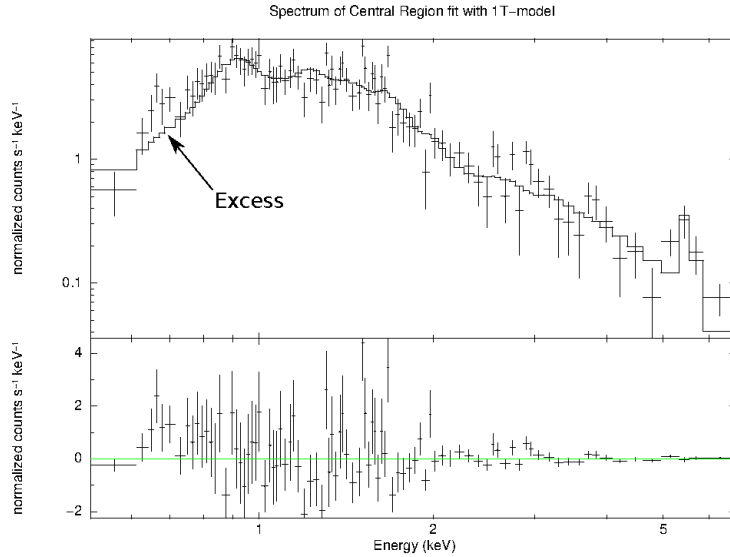


Figure 3.7: Absorbed, single-temperature model fit to the spectrum of the central 14 kpc. The model is a poor fit to the spectrum at low energies, with a clear excess between 0.6 and 0.7 keV. Including a second temperature component in the model improves the fit significantly.

### 3.4.2 Abundance Map

The central abundance in MS0735 is roughly  $0.7 Z_{\odot}$  and decreases with radius until it reaches  $0.2 - 0.3 Z_{\odot}$ . Regions of enhanced abundance are seen toward the end of the radio jets (black contours). A region with  $Z = 0.46 Z_{\odot}$  lies at the end of the jet pointing to the south. To the north the  $0.42 Z_{\odot}$  region lies beyond the extent of the radio jet. This observation is consistent with work done by Kirkpatrick et al. (2009) and Simionescu et al. (2009), who argued that cavities may lift metals to large radii as they rise through the cluster. Kirkpatrick et al. (in prep) measure excess iron emission along the direction of the radio jet in MS0735 out to a radius of  $\sim 300$  kpc. The high metallicity regions in Figure 3.5 are located at distances consistent with this iron radius.

## 3.5 Multiphase Gas

A single temperature thermal model provides a poor fit to the spectrum of the central 14 kpc below 1 keV. The spectrum, shown in Figure 3.7, has a soft excess located between 0.6 and 0.7 keV, resulting in a column density that approaches zero when allowed to vary. This is indicative of lower temperature gas located at the centre of the cluster. A second thermal component

was added to the original model, with abundances tied between the two thermal components and the column density fixed to the Galactic value. Applying an F-test, we find the two-temperature model provides a statistically significant improvement to the fit. The best-fitting temperatures are  $3.42_{-0.23}^{+0.26}$  keV and  $0.65 \pm 0.13$  keV, and the normalization of the cold component is 20 times smaller than that of the hot component. A single-temperature model is able to model the gas adequately at larger radii.

Assuming that the two gas phases are in pressure balance, the density ratio between the cold and hot phases is given by  $n_c/n_h = kT_h/kT_c$ . With temperatures of 3.4 and 0.65 keV, the cold gas would be a factor of 5 more dense than the hot gas. Gas masses can be calculated according to  $M = \mu m_p n V$ , where  $n \approx 2n_e$  is the total density and  $V$  is the volume of the gas. With a mean density of  $4.88 \times 10^{-2} \text{ cm}^{-3}$ , the mass of gas in the hot phase is  $1.7 \times 10^{10} M_\odot$ . Clumps of cold, dense gas do not fill the entire volume, so the mass of the cold phase cannot be calculated directly from this equation. Instead, the mass ratio can be determined from the normalizations of the XSPEC thermal models,  $K \propto n^2 V$ . Since  $M \propto n_e V$ , the cold gas is  $\frac{M_h}{M_c} = \frac{K_h n_c}{K_c n_h} \approx 100$  times less abundant than the hot gas, corresponding to a total mass of  $1.7 \times 10^8 M_\odot$ .

Bolometric X-ray luminosity is also determined directly from the thermal models, and is  $1.2 \times 10^{42} \text{ erg s}^{-1}$  for the cold phase and  $1.3 \times 10^{43} \text{ erg s}^{-1}$  for the hot phase. This gives a cooling time for the hot phase of  $6.4_{-0.8}^{+0.9} \times 10^8 \text{ yr}$ , which exceeds the projected cooling time,  $(2.4 \pm 0.1) \times 10^8 \text{ yr}$ , by a factor of almost 3 because of the large difference in central densities. The cold component, with a cooling time of  $1.3 \times 10^7 \text{ yr}$ , cools on a much shorter timescale than the hot phase. For steady, isobaric cooling the mass deposition rate,  $\dot{M}$  (Equation 1.4), is  $13 \pm 1 M_\odot \text{ yr}^{-1}$  for the warm phase and  $8 \pm 2 M_\odot \text{ yr}^{-1}$  for the cold phase. Both of these deposition rates greatly exceed the feeble star formation rate of  $< 0.25 M_\odot \text{ yr}^{-1}$  (McNamara et al., 2009). While cooling gas is apparently able to sustain the AGN, it is not fuelling star formation at an appreciable rate.

The radiative cooling of the central ICM can be suppressed by AGN heating provided cavity power exceeds the X-ray luminosity of the gas. The X-ray luminosities of the hot and cold components are  $(1.33 \pm 0.06) \times 10^{43}$  and  $(1.2 \pm 0.3) \times 10^{42} \text{ erg s}^{-1}$ , respectively. The mean power of the inner cavity system, discussed in Section 5, is  $5.2_{-1.8}^{+2.6} \times 10^{44} \text{ erg s}^{-1}$ , exceeding the combined X-ray luminosity in the central region by a factor of 40. While this provides ample power to suppress cooling, it is not clear how much of the energy is dissipated within the central 14 kpc.

AGN feedback can also suppress radiative cooling by physically removing the supply of low entropy gas from the centre of the cluster (Gitti et al., 2011). X-ray cavities have been shown to couple to the metal-rich central gas, dragging it toward large radii as the bubbles rise through the ICM (Kirkpatrick et al., 2009; Simionescu et al., 2009). The temperature map in Figure 3.6

shows that cool gas is displaced along the direction of the radio jet, implying that gas has been entrained by the radio jet or X-ray cavities and is being displaced from the cluster centre. Using abundance profiles along and perpendicular to the direction of the cavities, Kirkpatrick et al. (in prep) measure a gas outflow rate of  $150 \pm 80 M_{\odot} \text{ yr}^{-1}$  being dragged to a radius of  $\sim 300$  kpc. This large mass outflow rate can easily offset the combined  $21 M_{\odot} \text{ yr}^{-1}$  mass deposition rate.

### 3.6 Cooling Region

We define the region in which the cooling time is less than  $7.7 \times 10^9$  yr, the look-back time to  $z = 1$  for concordance cosmology, as the cooling region. In the absence of major mergers, some energy source must make up for the power radiated from within this region in order to suppress cooling in the long term. The cooling radius,  $r_{\text{cool}}$ , obtained from Figure 3.4 is 100 kpc, which is consistent with the XMM-Newton analysis of Gitti et al. (2007). A spectrum was extracted from a region with radius  $r_{\text{cool}}$  and was deprojected using spectra obtained from 3 overlying regions with the same radial width. The total luminosity within the cooling region was estimated by fitting this deprojected spectrum with the absorbed thermal model discussed in Section 3.2.1 and integrating the thermal component between 0.1 and 100 keV. The unabsorbed X-ray bolometric luminosity within this region is  $L_X(< r_{\text{cool}}) = (2.61 \pm 0.02) \times 10^{44} \text{ erg s}^{-1}$ .

The amount of gas that cools out of the ICM is estimated by adding an MKCFLOW component to the thermal model. The low temperature limit of this model was fixed to 0.1 keV in order to provide an upper limit on the amount gas cooling to low temperatures. The high temperature component was tied to the temperature of the MEKAL model and allowed to vary. Abundances were also tied between models. The resulting cooling luminosity,  $L_{\text{cool}} < 1.2_{-0.4}^{+0.5} \times 10^{43} \text{ erg s}^{-1}$ , is a small fraction ( $< 5\%$ ) of the total X-ray luminosity, and corresponds to  $< 22 \pm 8 M_{\odot} \text{ yr}^{-1}$  of gas cooling out of the ICM, which is broadly consistent with the  $40 \pm 10 M_{\odot} \text{ yr}^{-1}$  reported by Gitti et al. (2007). With a star formation rate of  $< 0.25 M_{\odot} \text{ yr}^{-1}$  (McNamara et al., 2009), only a small portion of gas actually cools out of the ICM and forms stars.

# Chapter 4

## The Powerful AGN Outburst

Now that the properties of the hot atmosphere have been quantified, we can determine the energetics of the powerful AGN outburst. Two enormous cavities, with diameters of  $\sim 200$  kpc, were identified in the X-ray surface brightness, and are filled by radio emission from a relativistic jet. The energy and power required to produce this outburst are calculated in Section 4.1, and are compared to radiative losses. Cool rims surround the cavities, and are studied in Section 4.2. A continuous, elliptical surface brightness edge encompassing the cavities was also detected in Chapter 3. This corresponds to a weak shock front, which we model in Section 4.3.

### 4.1 Cavities

X-ray images allow a direct measurement of cavity energetics to be made. The energy required to inflate a bubble in a hot atmosphere is given by its enthalpy,  $E_{\text{cav}} = 4pV$  (see Equation 1.4), where  $p$  is the pressure of the surrounding atmosphere. Cavity volume,  $V$ , can be determined from the projected size of the surface brightness depression and an assumption of the three-dimensional shape of the bubble. Three characteristic timescales are used to estimate the rise time of the bubble: the buoyancy time, sound-crossing time, and refill time (Equations 1.5, 1.6, and 1.7, respectively). Since all timescales are consistent within a factor of 2, we adopt the mean of these timescales as the age of the outburst. The mean power required to produce a cavity is then  $P_{\text{cav}} = 4pV/t_{\text{avg}}$ . This is likely an overestimate of the true outburst age, so the powers reported here are underestimates.

The projected sizes and positions of the cavities were determined by eye by fitting ellipses to the surface brightness depressions. The cavities are surrounded by bright rims that are presumably composed of displaced gas. The midpoint of these rims is taken for the measurement of

Table 4.1: List of cavity properties.

| Cavity   | $a$<br>kpc           | $b$<br>kpc           | $R$<br>kpc | $pV$<br>$10^{59}$ erg | $t_{\text{buoy}}$<br>$10^7$ yr | $t_{\text{cs}}$<br>$10^7$ yr | $t_{\text{refill}}$<br>$10^7$ yr | $t_{\text{avg}}$<br>$10^7$ yr | $P_{\text{cav}}$<br>$10^{44}$ erg s $^{-1}$ | $P_{\text{cav,tot}}$<br>$10^{44}$ erg s $^{-1}$ |
|----------|----------------------|----------------------|------------|-----------------------|--------------------------------|------------------------------|----------------------------------|-------------------------------|---|---|
| Outer NE | $109_{-15}^{+17}$    | $106_{-16}^{+17}$    | 150        | $110_{-40}^{+60}$     | 9.1                            | 12                           | 24                               | 15                            | $90_{-35}^{+50}$                            | $170_{-50}^{+60}$                               |
| Outer SW | $120_{-20}^{+10}$    | $100_{-25}^{+18}$    | 186        | $110 \pm 50$          | 11                             | 14                           | 25                               | 17                            | $80_{-40}^{+35}$                            |   |
| Inner NE | $13.3_{-2.0}^{+1.1}$ | $10.1_{-2.1}^{+2.5}$ | 19.3       | $0.9_{-0.4}^{+0.5}$   | 3.3                            | 1.9                          | 7.4                              | 4.2                           | $2.8_{-1.3}^{+1.6}$                         | $5.2_{-1.8}^{+2.6}$                             |
| Inner SW | $15.5_{-2.0}^{+2.3}$ | $10.5_{-3.3}^{+3.2}$ | 25.0       | $0.9_{-0.5}^{+0.7}$   | 4.1                            | 2.5                          | 7.8                              | 4.8                           | $2.4_{-1.3}^{+2.0}$                         |   |

cavity size. The inner (outer) edge of the rim is used to obtain a lower (upper) limit on the projected size of the cavity, which is used to determine the errors on cavity volume and subsequently on cavity enthalpy and power. The northeastern cavity is best fit by an ellipse with semi-major axis  $a = 109_{-15}^{+17}$  kpc, semi-minor axis  $b = 106_{-16}^{+17}$  kpc, and projected distance  $R = 150$  kpc with a position angle of  $19.4^\circ$  east of north. The southwestern cavity is best fit by an ellipse with  $a = 120_{-20}^{+10}$  kpc,  $b = 100_{-25}^{+18}$  kpc, and  $R = 186$  kpc with position angle  $202^\circ$  east of north. Table 4.1 summarizes the cavity properties and their derived energetics. The temperature, density, and pressure of the surrounding ICM is taken from Figure 3.4 at a radius corresponding to the centre of the cavities. Projected temperatures and deprojected densities are used in this analysis.

Cavity volumes are calculated using the geometric mean between oblate and prolate ellipsoids,  $V = \frac{4}{3}\pi(ab)^{3/2}$ . Upper (lower) limits on cavity volume are determined using the maximum (minimum) projected sizes, with volumes calculated in the same way as the mean volume. The total gas mass displaced by the cavities, assuming they are devoid of X-ray emitting material, is  $M_{\text{disp}} = 2n_e\mu m_p V$ . The electron density,  $n_e$ , is taken at a radius corresponding to the centre of the cavity. With volumes of  $15_{-6}^{+9} \times 10^{70}$  cm $^3$  and  $16_{-8}^{+7} \times 10^{70}$  cm $^3$  for the NE and SW cavities, respectively, the displaced gas masses are  $6_{-2}^{+3} \times 10^{11} M_\odot$  and  $5_{-3}^{+2} \times 10^{11} M_\odot$ . The  $pV$  work required to inflate the cavities is  $1.1_{-0.4}^{+0.6} \times 10^{61}$  erg for the NE cavity and  $1.1_{-0.5}^{+0.5} \times 10^{61}$  erg for the SW cavity.

The cavity ages estimated using the buoyancy, sound crossing, and refill timescales are listed in Table 4.1. The gravitational acceleration,  $g$ , used to calculate the buoyancy and refill timescales was determined using the MS0735 mass profile from Main et al. (in prep). In general the terminal velocity of bubbles is  $\sim 50\%$  of the sound speed (Rafferty et al., 2006). In MS0735, however, the large bubble volumes result in supersonic terminal velocities. Neglecting the bubble's expansion history in the buoyancy timescale therefore underestimates the true cavity age. We use the mean of the buoyancy, sound crossing, and refill timescales in order to estimate bubble age.

The ages of the NE and SW cavities are  $1.5 \times 10^8$  yr and  $1.7 \times 10^8$  yr, respectively. The

age of the surrounding shock front,  $1.1 \times 10^8$  yr (see Section 4.3), which should be comparable to the true cavity age, is shorter than the mean rise time. We therefore expect to have slightly overestimated cavity ages, so the calculated power is likely underestimated. The power required to inflate these bubbles is  $9_{-4}^{+5} \times 10^{45}$  erg s<sup>-1</sup> and  $8 \pm 4 \times 10^{45}$  erg s<sup>-1</sup> for the NE and SW cavities, respectively. The total enthalpy ( $4pV$ ) of these cavities is  $8.8_{-2.4}^{+3.2} \times 10^{61}$  erg, and the total power is  $1.7_{-0.5}^{+0.6} \times 10^{46}$  erg s<sup>-1</sup>.

The total cavity power of this AGN outburst exceeds the X-ray bolometric luminosity within the cooling radius,  $2.6 \times 10^{44}$  erg s<sup>-1</sup>, by more than a factor of 60, easily compensating for radiative losses. At a projected distance of  $\sim 150$  kpc, the majority of the cavity volume is located outside of the 100 kpc cooling region. Unless adiabatic losses from cosmic ray streaming account for a significant fraction of energy dissipation, most of the cavity enthalpy will be carried outside of the cooling region. If this energy is deposited within 1 Mpc, where the total gas mass is  $7 \times 10^{13} M_{\odot}$  (Main et al. in prep), the total cavity enthalpy heats the gas by 0.4 keV per particle.

Fuelling this outburst requires the accretion of  $5 \times 10^8 M_{\odot}$  of either cold molecular gas or the hot atmosphere at a rate of  $\sim 3 M_{\odot} \text{ yr}^{-1}$ . The detection of multiphase gas near the cluster nucleus has important repercussions for Bondi accretion. Cold, dense gas is able to accrete onto the central black hole much more efficiently than a warmer gas at the same pressure. With a density and temperature of  $0.24 \text{ cm}^{-3}$  and 0.65 keV, the cold component of the multiphase gas has a Bondi accretion rate of 0.14 for a  $5 \times 10^9 M_{\odot}$  black hole, which is far too small to fuel the AGN outburst. If MS0735 instead hosts an ultramassive black hole with mass  $7 \times 10^{10} M_{\odot}$  (McNamara et al., 2009), the Bondi accretion rate increases to  $\sim 30 M_{\odot} \text{ yr}^{-1}$ . While this is ample to power the outburst, the  $1.7 \times 10^8 M_{\odot}$  of cold gas falls below the minimum mass required to produce the observed energy. As a result, the large cavities in MS0735 cannot have been produced through the accretion of the hot atmosphere.

## 4.2 Cavity Rims

Bright rims of cool gas surround many cavity systems (e.g. Fabian et al. 2000; Nulsen et al. 2002; Blanton et al. 2001, 2011), and are also observed in MS0735. The brightest rim appears along the western edge of the NE cavity. A surface brightness profile, centred on the cavity, was created in order to determine the width of the rim. This profile, shown in Figure 4.1, is created from sectors with an  $80^{\circ}$  opening angle oriented to the west. Surface brightness is enhanced between  $\sim 100$  to 120 kpc, giving a rim width of 20 kpc.

A spectrum was extracted for the rim and fit with the absorbed thermal model discussed in Section 3.2.1. For comparison, a spectrum was extracted from a 20 kpc region just outside of

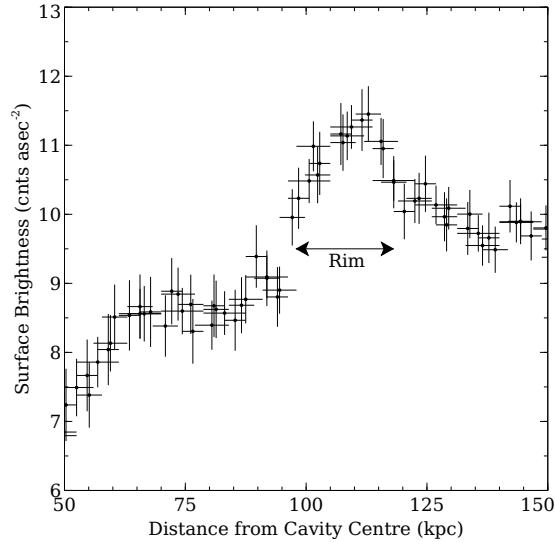


Figure 4.1: Surface brightness cut centred on the NE cavity and extending to the west with an  $80^\circ$  opening angle. Bright emission from rims surrounding the cavity is observed between 100 and 120 kpc. Profiles are shown for a variety of radial bin widths.

the rim with the same opening angle. The rim contains cooler gas than the surrounding gas, with  $kT = 5.7 \pm 0.4$  keV compared to the surrounding  $6.8_{-0.5}^{+0.6}$  keV. The ratio between densities can be determined directly from the normalization of the thermal model,  $K$ , and the volume of each region,

$$\frac{n_{\text{rim}}}{n_{\text{amb}}} = \sqrt{\frac{K_{\text{rim}} V_{\text{amb}}}{K_{\text{amb}} V_{\text{rim}}}}. \quad (4.1)$$

We find that the rim is a factor of  $1.18 \pm 0.03$  more dense than the surrounding gas. The pressure ratio between the rim and the ambient gas,  $1.0 \pm 0.1$ , implies that they are in pressure balance.

### 4.3 Shock

Radio jets launched by the AGN drive shock fronts into the ICM. MS0735 hosts a continuous, elliptical shock front that encompasses the outer pair of cavities (McNamara et al., 2005). This shock front is modelled as a spherically symmetric point explosion in an initially isothermal atmosphere in hydrostatic equilibrium. The surface brightness profile computed from the model is scaled to fit the preshock profile in the specified energy band. The postshock conditions are

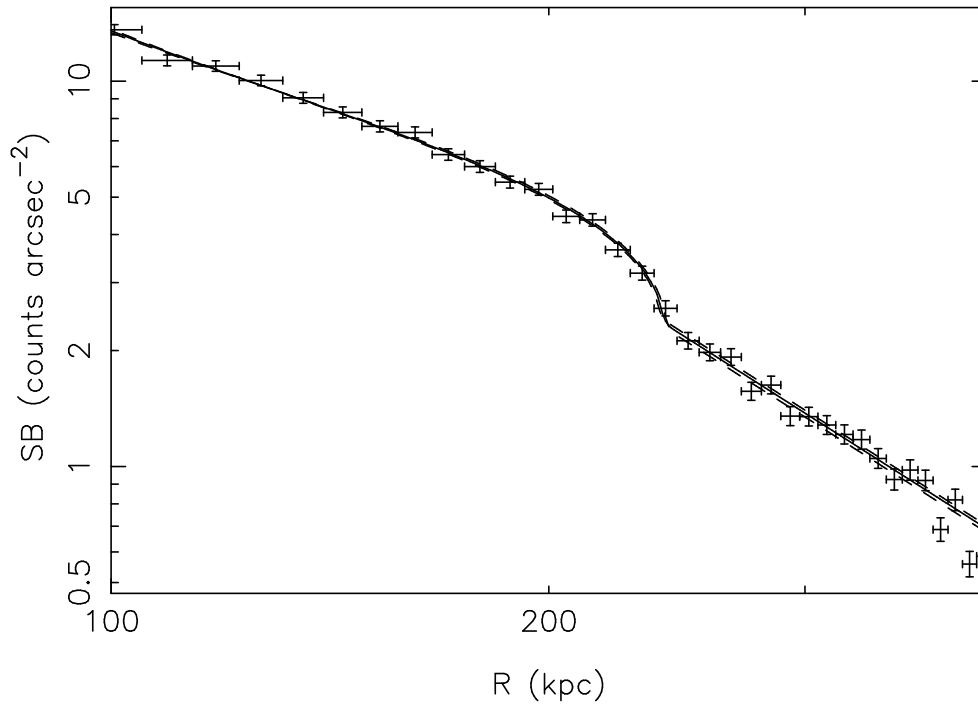


Figure 4.2: Projected surface brightness profile of the outer shock front compared to shock model predictions. The 0.5 – 7.0 keV surface brightness is measured in sectors centred around the semi-minor axis of the shock front with opening angles of  $30^\circ$  to the East and  $30^\circ$  to the West. This surface brightness profile is best fit by a shock with Mach number  $\mathcal{M} = 1.26^{+0.04}_{-0.09}$  at a radius of 245 kpc. The solid line shows the best fit from the shock model, which has been scaled to match the preshock surface brightness. The dashed lines show the fits from Mach numbers of 1.17 and 1.30.

then dictated by the Rankine-Hugoniot shock jump conditions for a given Mach number,  $\mathcal{M}$ . A detailed description of the analysis can be found in Nulsen et al. (2005).

The shock front is qualitatively fit by an ellipse with semi-major axis  $a = 320$  kpc, semi-minor axis  $b = 230$  kpc, and position angle of  $7^\circ$  east of north. We approximate the elliptical shock front using spherical symmetry by considering only small opening angles around the minor axis of the shock ( $30^\circ$ , roughly to the east and west). We are unable to accurately model the shock along the major axis because of the depression in postshock surface brightness caused by the large cavities. The  $0.5 - 7.0$  keV surface brightness profile extracted from these circular sectors is shown in Figure 4.2 and is best fit by Mach number  $\mathcal{M} = 1.26_{-0.09}^{+0.04}$  (90% confidence) at a radius of 245 kpc. This value is marginally ( $2\sigma$ ) below the  $1.41 \pm 0.07$  measured by McNamara et al. (2005). The difference is likely related to the improved precision yielded by the deeper observation, which provides a more accurate measurement of the pre- and post-shock surface brightness profiles and a more accurate characterization of the depth of the surface brightness discontinuity. The surface brightness of the preshock gas is best fit by the powerlaw  $r^{-\beta}$  with  $\beta = 2.48 \pm 0.06$ . The corresponding density profile, assuming constant temperature, is  $r^{-\eta}$  with  $\eta = 1.74 \pm 0.04$ .

From the Rankine-Hugoniot jump conditions, a Mach 1.26 shock causes a 25% increase in temperature. Projection effects obscure the jump, so that the expected temperature jump is only  $\sim 10\%$ . From Figures 3.3 and 3.4 the observed temperature jump,  $1.14 \pm 0.07$ , is within  $1\sigma$  of the expected jump. A map of the postshock temperature is provided in Figure 4.3, with the location of the shock front shown as the black ellipse. The postshock temperature is clearly highest along the major axis of the shock, reaching  $\sim 8$  keV to both the North and South but only  $\sim 7$  keV to the East and West. This is expected of an elliptical shock front, since the major axis must propagate faster and therefore has a higher Mach number. Due to the large uncertainties in temperature, the jumps along the major and minor axes are not significantly different. However, Figure 4.3 shows a clear azimuthal trend in temperature, which is indicative of an enhanced temperature jump along the major axis of the shock front.

The shock energy is determined from the point explosion model and depends on preshock temperature and density. The preshock properties are taken from the elliptical profiles in Figure 3.3, which trace the shock front well. The preshock temperature is specified as 6.5 keV with a density of  $1.85 \times 10^{-3} \text{ cm}^{-3}$  at 250 kpc, resulting in a shock energy of  $4 \times 10^{61}$  erg. Using the deprojected profiles in Figure 3.4 to determine the preshock conditions do not change the result, which is likely only accurate within a factor of  $\sim 2$ .

The main shortcomings of the shock model are in the assumptions of spherical symmetry and a point explosion. Spherical symmetry is a poor description of the elliptical shock front, so the shocked volume is underestimated. The AGN likely drives the shock through a continuous

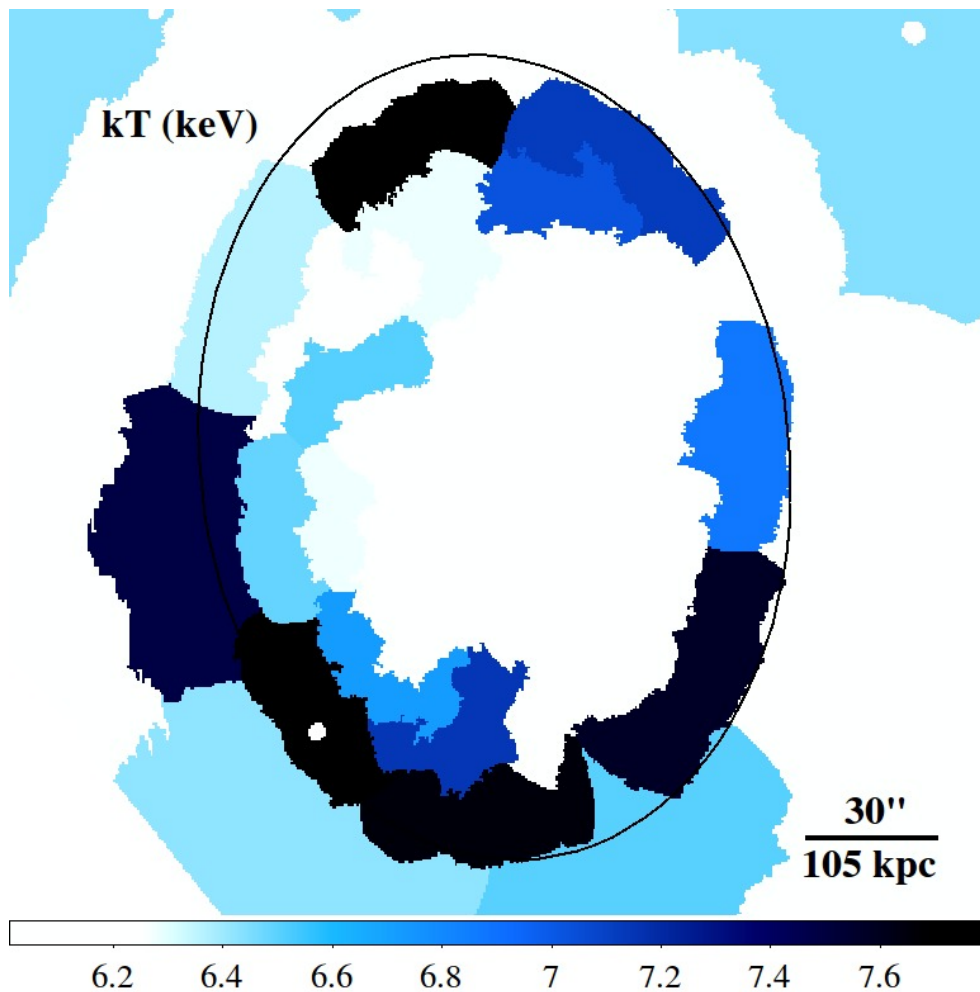


Figure 4.3: Same temperature map as in Figure 3.5, but scaled to focus on the shock front. The postshock temperature is highest along the major axis of the shock front, where the Mach number is highest.

injection of energy, which requires more energy than a point explosion in order to generate the same shock strength. The energy measured here,  $4 \times 10^{61}$  erg, is therefore an underestimate of the true shock energy. An improved shock model that does not assume spherical symmetry or a point explosion is required in order to improve the analysis of this weak shock.

The age of the shock determined by the model,  $1.1 \times 10^8$  yr, is comparable to the buoyancy and sound-crossing times of the cavities. Since they originate from the same AGN outburst, these ages are likely close to the true value. The shock power,  $E_{\text{shock}}/t_{\text{shock}} \approx 1.1 \times 10^{46}$  erg s<sup>-1</sup>, is slightly smaller than the total cavity power of  $1.7 \times 10^{46}$  erg s<sup>-1</sup>. Exceeding the X-ray luminosity within the cooling region by a factor of 40, the shock front also possesses ample power to offset radiative losses. Combined, the cavities and shock front are able to heat the ICM by 0.6 keV per particle within 1 Mpc, which provides a significant fraction of the 1 – 3 keV per particle required to preheat the cluster gas (Wu et al., 2000).

# Chapter 5

## Rejuvenated Outburst

The deep X-ray image reveals two smaller cavities or channels located along the radio jets in the inner 20 kpc of the BCG. Due to their small size relative to the larger cavities and their proximity to the cluster core, the cavities are difficult to disentangle from the gas presumably displaced by the large cavity system. The presence of a second pair of cavities is indicative of a rejuvenated AGN outburst. The inner edge of these cavities are traced by cool rims of displaced gas that are evident in the soft band (0.3 – 1.0 keV) image, shown in Figure 5.1 (left). This image was prepared in the same way as Figure 2.1, but with energies binned between 0.3 and 1.0 keV.

The right panel of Figure 5.1 shows five projections taken across the SW inner cavity. The black rectangle in the left panel of Figure 5.1 shows the projection corresponding to the middle profile. Counts in the 0.5 – 7 keV energy band were averaged over the 5 kpc width of the projection for each pixel along its length. Several of the profiles show a decrease in brightness, the most significant of which occurs  $\sim 22$  kpc from the cluster centre and reveals a 10 – 20% deficit in counts relative to the surrounding bright rims. The decrease in counts toward the NE cavity is much smaller than is seen in the SW cavity, merely flattening instead of producing a clear deficit. This difference likely results from the projection into our line of sight of emission from dense gas, non-uniformly distributed in the cavity rims.

The projected sizes of the two inner cavities are determined in the same manner as the outer cavities (see Section 4.1). The white ellipses in Figure 5.1 (left) show the cavity sizes adopted here, which use the middle of the rims to determine the mean cavity volume. This approach gives a projected size of  $a = 13.3^{+1.1}_{-2.0}$  kpc,  $b = 10.1^{+2.5}_{-2.1}$  kpc for the inner NE cavity and  $a = 15.5^{+2.3}_{-2.0}$  kpc,  $b = 10.5^{+3.2}_{-3.3}$  kpc for the inner SW cavity. Volumes for these cavities are calculated using the geometric mean between oblate and prolate ellipsoids, or  $V = \frac{4\pi}{3}(ab)^{3/2}$ . At projected distances of 19.3 and 25.0 kpc from the cluster centre, these cavities displace  $8.2 \times 10^9 M_{\odot}$  and

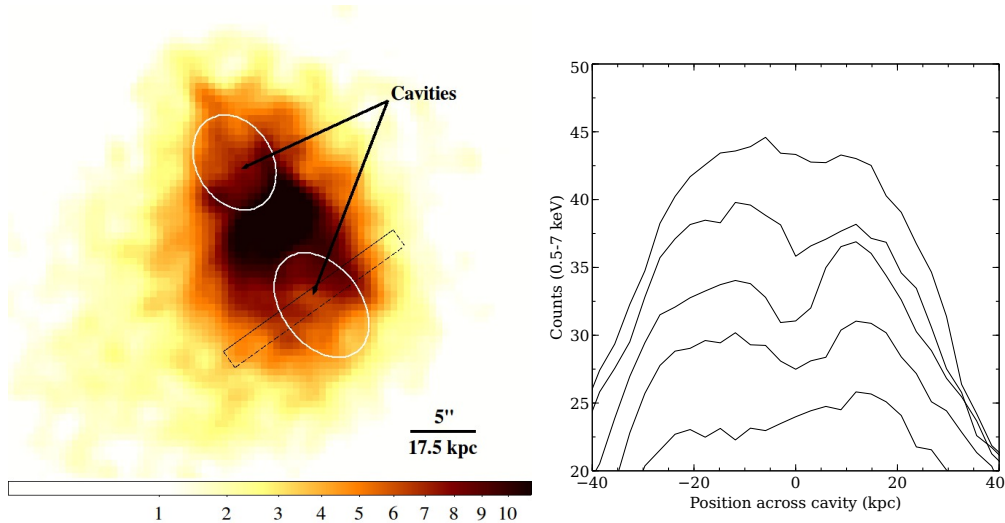


Figure 5.1: *Left*: Soft band (0.3 – 1.0 keV) image in units of counts pixel<sup>-1</sup>, Gaussian-smoothed with a 1.5'' kernel radius. Two regions of low surface brightness are visible in this image, which we interpret as a pair of cavities originating from a recent AGN outburst. *Right*: Counts from the 0.5 – 7 keV band for a series of linear projections lying across the SW inner cavity. The projections are taken at a series of radii from the cluster centre, lying roughly perpendicular to the radial direction. The region associated with the middle profile is shown in the left panel as the rectangle. The position across the cavity starts from the NW and runs toward the SE.

$7.7 \times 10^9 M_{\odot}$  of gas in the ICM, respectively.

The mechanical energy required to inflate these cavities,  $pV$ , is  $9_{-4}^{+5} \times 10^{58}$  erg for the inner NE cavity and  $9_{-5}^{+7} \times 10^{58}$  erg for the inner SW cavity. The mean age of the bubbles,  $4.8 \times 10^7$  yr and  $4.2 \times 10^7$  yr, give cavity powers of  $2.8_{-1.3}^{+1.6} \times 10^{44}$  erg s<sup>-1</sup> and  $2.4_{-1.3}^{+2.0} \times 10^{44}$  erg s<sup>-1</sup>, respectively. The total mechanical energy ( $4pV$ ) and power for this outburst are therefore  $7.2_{-2.6}^{+3.4} \times 10^{59}$  erg and  $5.2_{-1.8}^{+2.6} \times 10^{44}$  erg s<sup>-1</sup>. This cavity power exceeds radiative losses within the cooling region ( $2.6 \times 10^{44}$  erg s<sup>-1</sup>) by a factor of 2 and is 30 times smaller than the outer cavity power, implying that AGN power varies significantly over time. While feeble compared to the outer cavities, the inner cavities are comparable in power to the bubbles in Perseus.

Despite the ample energy in the outer outbursts, a rejuvenated AGN outburst is required in order to continue to offset radiative losses (see e.g. Perseus: Fabian et al. 2006, M87: Forman et al. 2007, Hydra A: Nulsen et al. 2005). The outburst interval in MS0735, given by the difference in mean bubble ages, is  $1.1 \times 10^8$  yr. This value ranges between a minimum of  $6 \times 10^7$  yr when the buoyancy time is used to a maximum of  $1.7 \times 10^8$  yr with the refill timescale. Each of these values is shorter than the central cooling time,  $6.4_{-0.8}^{+0.9} \times 10^8$  yr. The AGN outbursts

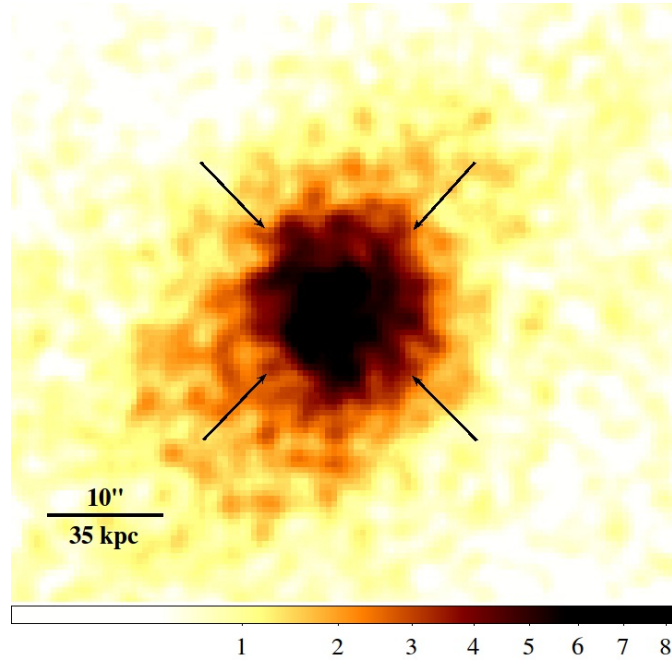


Figure 5.2: Hard band (3 – 7 keV) image in units of counts  $\text{pixel}^{-1}$ , smoothed with a two-dimensional Gaussian with a  $1.5''$  kernel radius. The arrows indicate a circular feature that is reminiscent of the weak shock in M87.

therefore occur on short enough timescales to prevent the majority of the ICM from cooling. Repeated heating of the central gas supplies enough energy to prevent cooling, and may explain the lack of star formation in the system (McNamara et al., 2009).

Powering this outburst is considerably easier than the large AGN outburst, requiring only  $4 \times 10^6 M_{\odot}$  of gas accreted at an average rate of  $0.09 M_{\odot} \text{ yr}^{-1}$ . Bondi accretion of the cold component of the multiphase atmosphere and the accretion of cold molecular gas are both capable of fuelling this outburst. As discussed in Section 4.1, the Bondi accretion rate is  $0.14 M_{\odot} \text{ yr}^{-1}$  for the multiphase gas. Furthermore, with a mass of  $1.7 \times 10^8 M_{\odot}$ , more than enough gas is present to fuel the outburst. We note that the hot phase, which is 100 times more massive, has a Bondi accretion rate of only  $2.3 \times 10^{-3} M_{\odot} \text{ yr}^{-1}$ , so cannot power the outburst unless MS0735 hosts an ultramassive black hole.

## 5.1 Spectrally Hard Features: An Inner Shock?

Weak shocks are typically produced alongside cavities in an AGN outburst. The gas warmed by shock heating can be traced using a hard band image (Forman et al., 2007), which excludes the portion of the X-ray spectrum that is only weakly dependent on temperature (see Figure 1 of Arnaud 2005). We produce a hard band image by binning cluster emission between 3 and 7 keV. The hard emission, shown in Figure 5.2, is fairly circular, with extended emission lying perpendicular to the jet axis. This morphology is quite different than the cooler gas traced by the soft band (Figure 5.1), which shows emission extending along the jet axis.

The arrows in Figure 5.2 point to a circular feature that is reminiscent of the shock front in M87 (Forman et al., 2007). A jump in surface brightness is observed at this location, but it is marginal and depends strongly on radial binning. We therefore cannot conclusively determine if this feature corresponds to a shock front. If it is a shock front, then, approximating the density jump from the surface brightness jump, it would have a Mach number of approximately 1.1. With a radius of 30 kpc the energy of the shock front is  $\sim 3 \times 10^{59}$  erg, which is a factor of 2 smaller than the total mechanical energy required to inflate the associated bubbles. The age of this shock is  $2.6 \times 10^7$  yr for a preshock temperature of 4 keV, which translates to a power output of  $\sim 4 \times 10^{44}$  erg s<sup>-1</sup>. This shock power is comparable to the total cavity power for the rejuvenated outburst as well as the X-ray bolometric luminosity within the cooling region.

# Chapter 6

## AGN Outburst Time Dependence

MS0735 is one among several clusters and groups with two or more pairs of radio cavities embedded in their hot atmospheres. These systems are particularly interesting because they permit a direct indication of AGN power variability over time and the time interval between outbursts, which should be shorter than the cooling time if AGN are regulating cooling (Dunn & Fabian, 2006; Rafferty et al., 2008; Bîrzan et al., 2012). Those known to us are listed in Table 6.1. We compare the time interval between outbursts in these systems to central cooling time and cavity heating time. We note that this archival sample is heavily biased by selection, as only large bubbles are detectable and multiple outbursts can only be detected for a select range of outburst intervals. There is likely a range in cavity sizes and ages that we are currently unable to detect (McNamara & Nulsen, 2007).

Outburst interval is determined from the difference in ages between inner and outer cavities, with buoyancy times used to determine bubble ages. Outburst intervals are also determined from the period of weak shocks and sound waves. A factor of 2 uncertainty is attributed to all outburst intervals. For bubbles this roughly translates to calculating bubble ages from the sound crossing time and refill time and using those estimates as lower and upper bounds, respectively. The outburst intervals presented here, determined from cavity ages, range from  $6 \times 10^6$  yr in M87 to  $1.8 \times 10^8$  yr in Hydra A. The mean outburst interval of these points is  $6_{-1}^{+2} \times 10^7$  yr, while sound waves occur on much shorter timescales, with a mean period of  $0.7_{-0.2}^{+0.5} \times 10^7$  yr.

Central cooling times are obtained from the Rafferty et al. (2008) and Cavagnolo et al. (2009) samples, and are plotted against outburst interval in Figure 6.1. Outburst intervals determined from bubble ages are plotted as circles, while those determined from weak shocks or sound waves are plotted as triangles. The points are colour-coded based on the central resolution element. Nearby systems, where the achievable resolution is  $< 1$  kpc, are shown in white. Grey points

Table 6.1: Sample of systems with multiple AGN outbursts.

| Cluster        | Outburst Type <sup>a</sup> | Reference                   |
|----------------|----------------------------|-----------------------------|
| Perseus        | 1, 2                       | Fabian et al. (2006)        |
| M87            | 1, 2                       | Forman et al. (2007)        |
| MS 0735.6+7421 | 1                          | This work                   |
| Hydra A        | 1                          | Wise et al. (2007)          |
| HCG 62         | 1                          | Rafferty et al. (2013)      |
| A2052          | 1                          | Blanton et al. (2009, 2011) |
| A2199          | 1                          | Nulsen et al. (2013)        |
| NGC 5813       | 1                          | Randall et al. (2011)       |
| NGC 5846       | 1                          | Machacek et al. (2011)      |
| A3581          | 1                          | Canning et al. (2013)       |
| Centaurus      | 2                          | Sanders & Fabian (2008)     |

<sup>a</sup>Type of outburst used to calculate outburst interval. 1: Cavities, 2: Shocks or sound waves.

correspond to a resolution of 1 – 5 kpc and black points are for systems with a resolution that exceeds 5 kpc. The clear separation between these points can be attributed to resolution (Peres et al., 1998). A consistent physical scale would shift the grey and black points to the left, but they tend to be hotter systems so would still have a longer central cooling time than most of the white points. Multiple points are shown for Hydra A, M87, and NGC 5813 because they host bubbles from 3 AGN outbursts, corresponding to 2 outburst intervals.

Cavities cannot heat the central gas once they have risen beyond a certain radius, so another heating event is required in order to offset cooling flows over the long term. As a result, AGN must rejuvenate on a timescale comparable to or shorter than the central cooling time. After accounting for resolution, Figure 6.1 shows that outburst interval is shorter than or consistent with the mean central cooling time for each system in our sample, implying that AGN outbursts rejuvenate rapidly enough to continually suppress cooling flows (see Rafferty et al. 2008). The period of weak shocks and sound waves in M87 (Forman et al., 2007), Perseus (Fabian et al., 2006), Centaurus (Sanders & Fabian, 2008), and A2052 (Blanton et al., 2009) are each an order of magnitude smaller than their central cooling time, implying that heating from repeated weak shocks may also play an important role in suppressing cooling flows in the centres of clusters.

The mean cooling time for this sample of groups and clusters is  $19_{-2}^{+4} \times 10^7$  yr, which is a factor of 3 larger than the mean outburst interval. The white points in Figure 6.1 have a much shorter mean cooling time,  $5.0_{-0.6}^{+0.7} \times 10^7$  yr, than the points in grey,  $30_{-5}^{+8} \times 10^7$  yr. These points also have shorter outburst intervals, with a mean outburst interval of  $2.9_{-0.7}^{+1.5} \times 10^7$  yr compared

to  $8_{-2}^{+4} \times 10^7$  yr. Therefore the nearest systems, which have shorter central cooling times, also have shorter outburst intervals. This effect may be influenced by resolution, where the closer system have shorter outburst intervals because it is easier to detect small cavities.

We define cavity heating time as the amount of time that cavity enthalpy is able to offset radiative losses,  $t_{\text{heating}} = 4pV/L_X(< r_{\text{cool}})$ . A large outburst offsets cooling for longer times, which could translate to a longer outburst interval. Cavity heating time is compared to outburst interval in Figure 6.2. For the factor of 30 range in outburst intervals, cavity heating time spans 4 orders of magnitude. We find that outburst interval is shorter than cavity heating time for 8 of the 13 points in our sample. We note that  $t_{\text{heating}}$  is likely underestimated in NGC 5846 by a factor of a few, as Machacek et al. (2011) report the X-ray luminosity within 200 kpc while the cooling radius is approximately 25 kpc (Cavagnolo et al., 2009).

The majority of systems in Figure 6.2 (8 of 13) have an outburst interval shorter than their cavity heating time, indicating that heating is continually able to offset radiative cooling over the age of the cluster. Furthermore, the presence of weak shocks and sound waves imply that cavity enthalpy is only a lower limit on the total energy of an AGN outburst, so an AGN outburst will be able to heat the system for longer than the heating time shown in Figure 6.2. Conversely, the largest of these outbursts (Hydra A, MS0735) are depositing some of their energy beyond the cooling radius, resulting in an overestimated heating time. Correcting for this effect would decrease the heating times in these systems, moving them closer to the line of equality. The very small range in outburst intervals relative to the 4 order of magnitude range in heating times suggests that any relationship between these timescales is weak. A much larger sample is required in order to draw any conclusions. The current sample is heavily biased toward nearby systems with large outbursts, and only a small range in outburst interval is detectable.

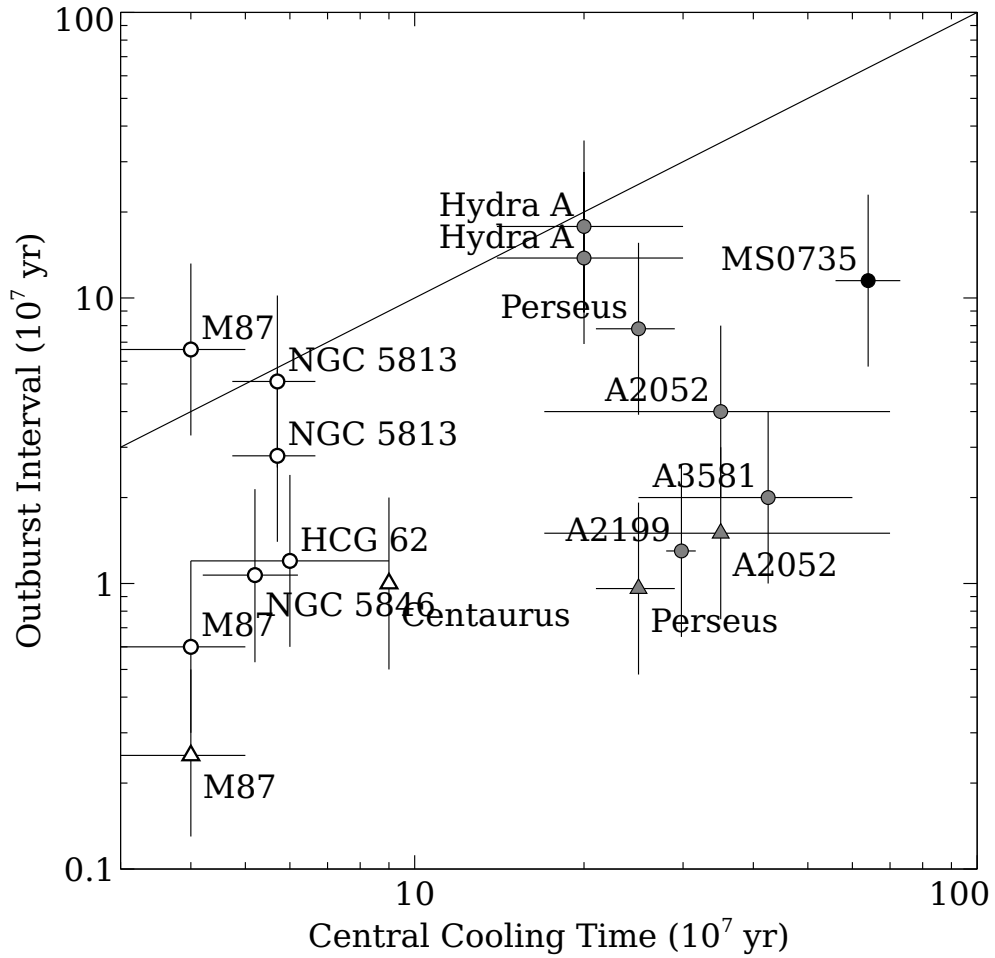


Figure 6.1: AGN outburst interval plotted against central cooling time. Circles represent outburst intervals obtained from cavity ages while triangles are the estimates from sound waves or repeated weak shocks. The points are colour-coded based on the resolution, where white points are cooling times from the inner 1 kpc, grey are from the inner 5 kpc, and black are from the inner 10 kpc. In each system the duty cycle is shorter than the central cooling time. The line of equality between duty cycle and central cooling time is shown.

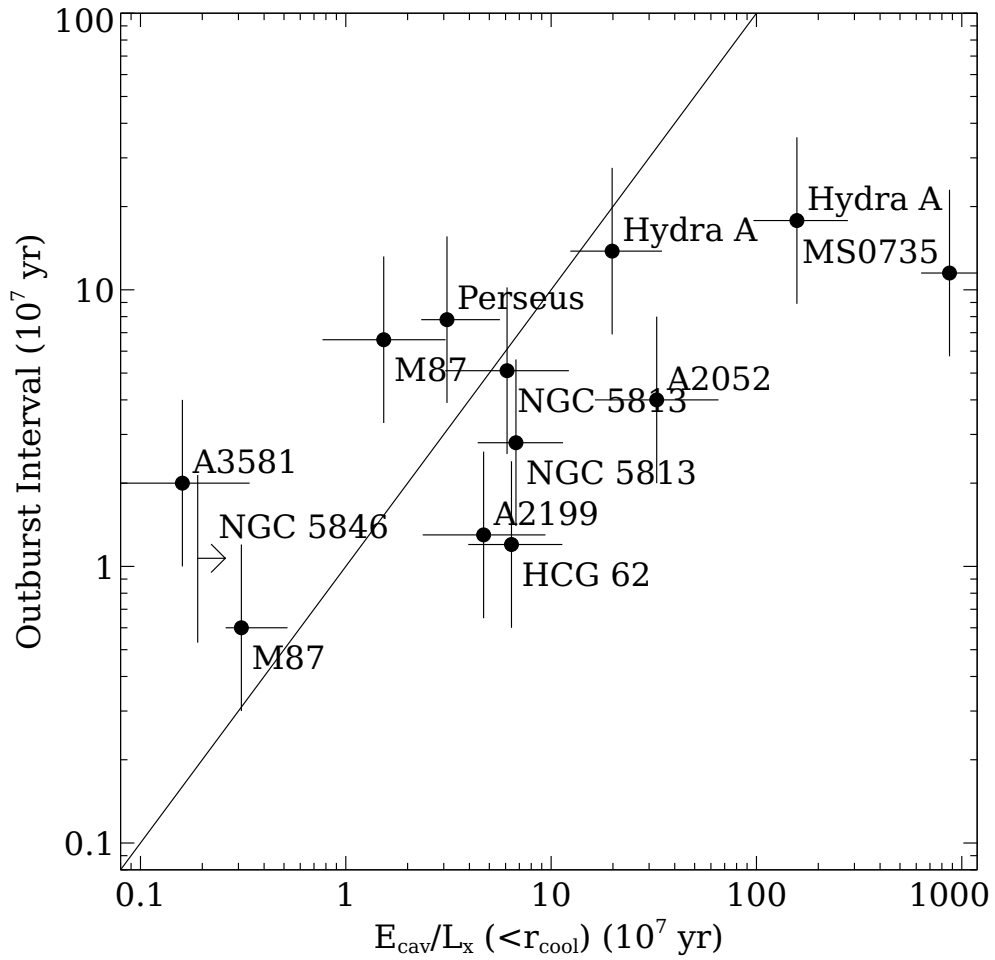


Figure 6.2: AGN outburst interval plotted against heating time – the amount of time that the outer cavity is able to compensate for radiative losses. Only outburst intervals determined from cavities are included in this plot. The solid line is the line of equality between the two timescales.

# Chapter 7

## H $\alpha$ Nebula in the Brightest Cluster Galaxy

Heating from active galactic nuclei suppresses the bulk of a cooling flow, but residual cooling of tens to hundreds of solar masses per year is still observed in many systems. This gas rapidly condenses out of the intracluster medium, forming atomic gas that is spatially coincident with the filamentary structure of the X-ray emitting gas (Fabian et al., 2008) and eventually forms molecular gas and fuels star formation. Accretion of either this cold gas or of the hot atmosphere onto the central black hole is required in order to power AGN outbursts. A cold disk discovered in Hydra A may be an indication that AGN outbursts are controlled by the accretion of cold gas (Hamer et al., 2014). Rotation in many other systems may further implicate cold gas as the source of fuel in the AGN feedback process (Hamer et al. in prep).

In general the gaseous nebulae in BCGs are relatively quiescent, hosting simple and ordered spatial and kinematic morphologies (Hamer et al. in prep). A smaller fraction of systems, however, are disrupted either through galaxy-galaxy interactions or by AGN feedback. Recent ALMA observations have revealed a bipolar outflow of molecular gas located behind the buoyantly rising bubbles (McNamara et al., 2014; Russell et al., 2014), implying that systems with powerful AGN may be capable of displacing the reservoir of cold gas. If AGN feedback does affect the morphology of a gaseous nebula, the effect should be apparent in MS0735, which hosts the most energetic AGN outburst known.

In this chapter we present preliminary results from a Gemini observation of the central cluster galaxy in MS0735. We outline the data reduction along with steps that can be taken to improve it. We then present our spectral fitting method and use it to create maps of flux, velocity, and velocity dispersion. Finally, a preliminary interpretation of these maps is presented, with a focus on how the dynamics of the gas are affected by the AGN feedback process.

## 7.1 Observations

Spatially resolved spectroscopy of the brightest cluster galaxy (BCG) in MS0735 was obtained using the integral field unit (IFU) on the northern Gemini Multi-Object Spectrograph (GMOS-N). Five science observations, each 30 minutes in duration, were obtained on April 15th and 16th, 2012 – three on April 15th and two on April 16th. Short (5 second) observations of the dome flat were interspersed with the science observations. This consists of observing a uniformly-illuminated screen in order to perform flat-fielding. Observations of the standard star, Wolf 1346, were obtained on April 16th following the science observations. Another observation of the dome flat was obtained at this time. The twilight was observed towards the end of the April 15th observing period. Arc flats, which are used for wavelength calibrations, were exposed at the end of each day.

The integral field unit on GMOS consists of 1500 hexagonal lenslets, each coupled to an optical fiber. This lenslet array divides the sky into 1500 pieces, with a grating producing a spectrum for each lenslet. The science field-of-view is sampled by 1000 lenslets, and corresponds to a 7 arcsec x 5 arcsec field of view. The remaining 500 lenslets are interspersed among the science lenslets, and are used to observe the sky roughly 1 arcmin away from the target. When operating in one-slit mode, which we employed for our observations, only half of the lenslet array is used in exchange for extended wavelength coverage. The 500 object lenslets give a field-of-view of 3.5 arcsec x 5 arcsec, with 250 lenslets used for the sky observation. The observations conducted here were performed using only the red slit, which has a wavelength coverage of  $\sim 6600 - 9500\text{\AA}$ . The redshifted  $H\alpha$  line ( $[\text{H I}]\lambda 6563$ ) is located at  $7980\text{\AA}$ , roughly in the centre of the red slit's wavelength coverage.

## 7.2 Data Reduction

Reduction of the IFU data was performed using the Gemini pipeline in the IRAF environment. All observations are first corrected for overscan – a constant offset among all pixels that varies between observations – and bias – constant pixel-to-pixel offsets introduced when the detector is read out. Gemini provides a master bias file for each science program. However, this file commonly fails to remove the bias accurately (Swinbank, priv. comm.), and it was found to be problematic in our data reduction. As a result, only the overscan subtraction was applied.

The overscan and bias is first removed from the dome flats, and spectra are extracted for each lenslet. Dome flats are exposures of a uniformly-illuminated screen. Any variation in the image is an artifact of the detector, and is caused by a change in quantum efficiency or from the optics

not illuminating the detector uniformly. These files can then be flat-fielded by dividing this image into the others.

The conversion from channel to wavelength is non-linear and must be determined using a standard lamp or arc. The arc exposures were flat-fielded using the appropriate dome flat and spectra were extracted from each aperture. The known spectral lines in each spectrum were fit and the lines positions were compared to the Gemini standard for the red slit, CuAr R400 (780 nm). This allows each energy channel to be translated directly into wavelength. Instrumental broadening contributes to the line-widths in the observed arcs. This effect is typically small, but must be taken into account. This step has not yet been performed, so all velocity dispersions, which are determined from the width of the H $\alpha$  and [NII] lines, are systematically high.

The science observations can now be reduced by applying the overscan subtraction, bias removal, flat-fielding, and wavelength calibration. Cosmic-ray removal is also applied at this stage of the reduction. Each fiber block is then sky-subtracted using the adjacent block of sky fibers. This reduction step also commonly encounters errors (Swinbank, priv. comm.), though it is not clear if the problem is significant in this data reduction. In the future this step will need to be checked more thoroughly.

Reduction of the standard star is conducted in the same way as the science observation. A single spectrum is obtained by summing the spectrum from each aperture. Comparison of this spectrum to the calibration data of the standard star allows the detector sensitivity as a function of wavelength to be computed. This sensitivity curve is then applied to the science data in order to perform the flux calibration. The flux-calibrated spectra from each aperture are mapped onto the sky using the GFCUBE task. The resulting 3D datacube shows an image of the sky for each wavelength slice. Finally, a datacube of the mean flux was created by averaging the datacube for each science observation.

A datacube was also created for the standard star, Wolf 1346. Each pixel, which corresponds to an angular size of 0.05 arcsec, was integrated over the entire wavelength coverage to obtain a flux map. Two flux profiles were obtained using projections oriented along the north-south and east-west axes, respectively, extending to the edge of the field-of-view. Fitting a Gaussian to each flux profile gives a mean full-width at half-maximum of 0.8 arcsec. Since the standard star is a white dwarf and should not be resolved by our observation, this measurement represents the seeing. We are therefore not able to resolve any structures smaller than 0.8 arcsec in diameter. Changing the spatial sampling to 0.1 arcsec per pixel was found to give a consistent seeing.

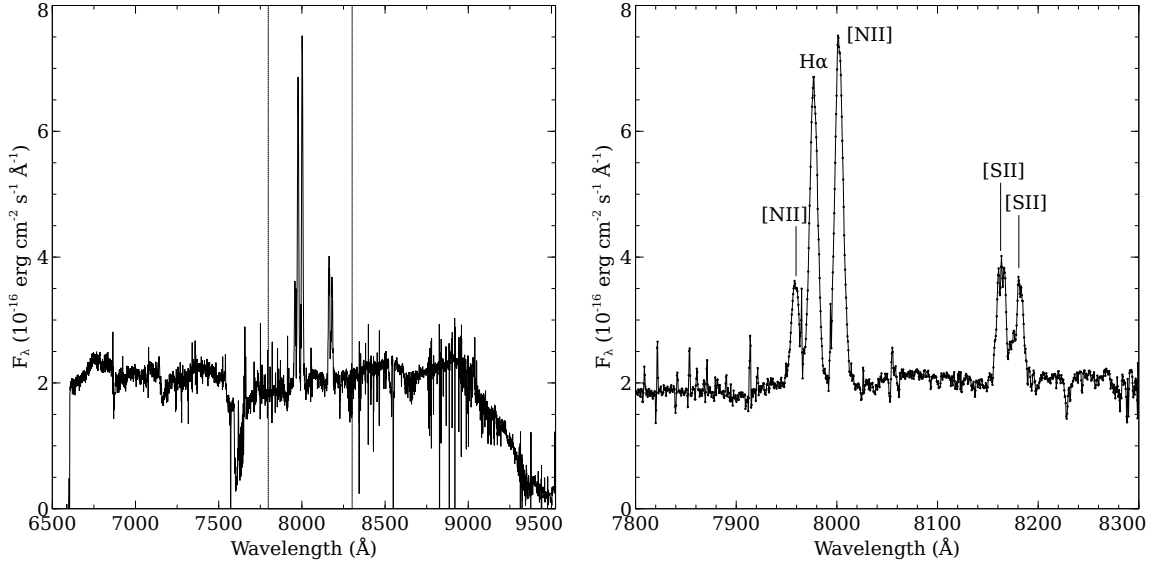


Figure 7.1: Spectrum of the central 1 arcsec radius. The dotted lines indicate the wavelength region shown in the right panel.

### 7.3 Spectral Fitting

A sample spectrum, extracted from a region 10 pixels (1 arcsec) in radius centred on the continuum maximum, is shown in Figure 7.1. The decrease in  $F_\lambda$  above  $9000\text{\AA}$  is the result of a poor extrapolation of the fit to the sensitivity curve and is not used in the analysis. The dotted box is centred around the emission lines and indicates the wavelength range of the right panel of Figure 7.1. Five emission lines are clearly identifiable in this spectrum:  $H\alpha$ ,  $[\text{NII}]\lambda\lambda 6548, 6583$ , and  $[\text{SII}]\lambda\lambda 6716, 6731$ . No other emission lines are detected in the spectrum with high significance.

The properties of each line, including the flux, gas velocity, and velocity dispersion, are determined by fitting a Gaussian of the form

$$F_\lambda = A \exp \left[ \frac{-1}{2} \left( \frac{\lambda - B}{C} \right)^2 \right] \quad (7.1)$$

to the line. The flux of the line is then given by

$$F_{\text{line}} = \int F_\lambda d\lambda = \sqrt{2\pi} AC. \quad (7.2)$$

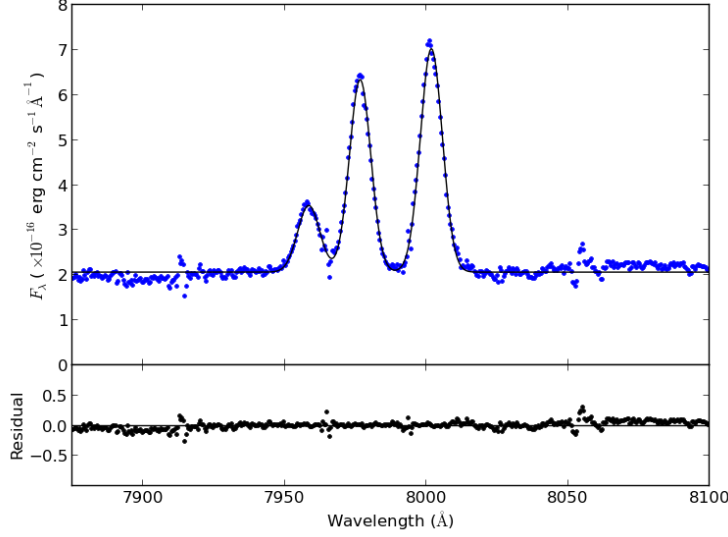


Figure 7.2: Spectrum of the central 1 arcsec radius between 7850 and 8100Å. The spectrum is fit by the sum of three Gaussians, with a constant offset for the continuum emission.

The gas velocity is determined from the doppler shift according to

$$\frac{v}{c} = \frac{B - \lambda_0}{\lambda_0}, \quad (7.3)$$

where  $c$  is the speed of light and  $\lambda_0$  is the rest wavelength of the line, redshifted to the systemic velocity of the cluster ( $z = 0.216$ ). In this convention, positive velocities correspond to a redshift, where the gas is travelling away from the observer. Velocity dispersion,  $\sigma$ , is calculated from the full-width at half-maximum (FWHM) according to

$$\frac{\sigma}{c} = \frac{\text{FWHM}}{B} = 2\sqrt{2 \ln 2} \left( \frac{C}{B} \right). \quad (7.4)$$

The  $H\alpha$  and  $[\text{NII}]$  lines must be fit simultaneously due to their proximity. A constant offset is added to the three Gaussian functions in order to account for continuum emission. Figure 7.2 shows the best fit to the lines. While the continuum would be better fit by a first-order polynomial, the constant provides a sufficient fit to the data for our purposes. The  $H\alpha$  flux in this region is  $4.1 \times 10^{-15} \text{ erg cm}^{-2} \text{ s}^{-1}$  and corresponds to a luminosity of  $5.5 \times 10^{41} \text{ erg s}^{-1}$  for a luminosity distance of  $D_L = 1070 \text{ Mpc}$ . The  $[\text{NII}]\lambda 6548$  and  $[\text{NII}]\lambda 6583$  fluxes are  $1.5 \times$

$10^{-15}$  and  $4.8 \times 10^{-15}$  erg cm $^{-2}$  s $^{-1}$ , respectively. Donahue et al. (1992) report an H $\alpha$ + [NII] flux of  $9 \pm 2 \times 10^{-15}$  erg cm $^{-2}$  s $^{-1}$ , which is roughly consistent with the combined flux of  $12 \times 10^{-15}$  erg cm $^{-2}$  s $^{-1}$  measured here.

At a redshift of  $z = 0.216 \pm 0.003$  (Stocke et al., 1991), the rest wavelength of the H $\alpha$  line in MS0735 is  $7980 \pm 20 \text{ \AA}$ . The observed H $\alpha$  line in the central 1 arcsec is centred around  $7976.5 \text{ \AA}$ , corresponding to a blueshift of  $\sim 150$  km s $^{-1}$ . Comparable velocities are measured for both [NII] lines. Since the redshift measurement is only accurate to  $(\delta z)c = \pm 900$  km s $^{-1}$ , we adopt this measurement as the central velocity of the BCG. All velocity maps presented in the following section are measured relative to this velocity, which is equivalent to a redshift of 0.2154.

## 7.4 Maps

A spectrum was extracted from each spatial pixel in the IFU datacube in order to create maps of flux, velocity, and velocity dispersion. The datacubes were created such that 1 pixel corresponds to an angular size of 0.1 arcsec. Only the H $\alpha$  and [NII] lines, fit by the triple-Gaussian described above, were used to create the maps. The maps, which are shown in Figures A.3-A.5, are oriented with north upwards and east to the left.

At optical wavelengths the continuum is dominated by free-bound emission from the recombination of nuclei with electrons (Osterbrock & Ferland, 2006). The continuum map, shown in Figure 7.3 (top), was constructed simply from the constant offset added to the Gaussian emission lines. The continuum is fairly circular and is sharply peaked in the centre, reaching a maximum value of  $10^{-18}$  erg cm $^{-2}$  s $^{-1}$  \AA $^{-1}$  at the location marked by the white 'x'.

The map of H $\alpha$  flux is shown in Figure 7.3 (bottom), in units of  $10^{-17}$  erg cm $^{-2}$  s $^{-1}$ . The peak in the H $\alpha$  emission is marked by the white '+'. Summing the flux for each pixel in the central 1 arcsec yields an H $\alpha$  flux of  $4.0 \times 10^{-15}$  erg cm $^{-2}$  s $^{-1}$ , consistent with the  $4.1 \times 10^{-15}$  erg cm $^{-2}$  s $^{-1}$  obtained from extracting a spectrum directly from the datacube and indicating that flux maps are able to accurately reproduce the flux of a region that spans several pixels. Over the entire  $3.5 \times 5$  arcsec $^2$  field-of-view we recover an H $\alpha$  flux of  $7.9 \times 10^{-15}$  erg cm $^{-2}$  s $^{-1}$ , corresponding to an H $\alpha$  luminosity of  $1.1 \times 10^{42}$  erg s $^{-1}$ . This exceeds the flux reported by Donahue et al. (1992) by almost a factor of 2, though Donahue et al. (1992) note that their reported H $\alpha$ + [NII] flux may be somewhat underestimated.

While the continuum appears to be spherically symmetric, the morphology of the H $\alpha$  nebula is not as simple. Instead, the H $\alpha$  emission is fairly circular in the centre but extends upward with a position angle of  $10^\circ$  west of north. Ellipticity along this axis was also found by McNamara

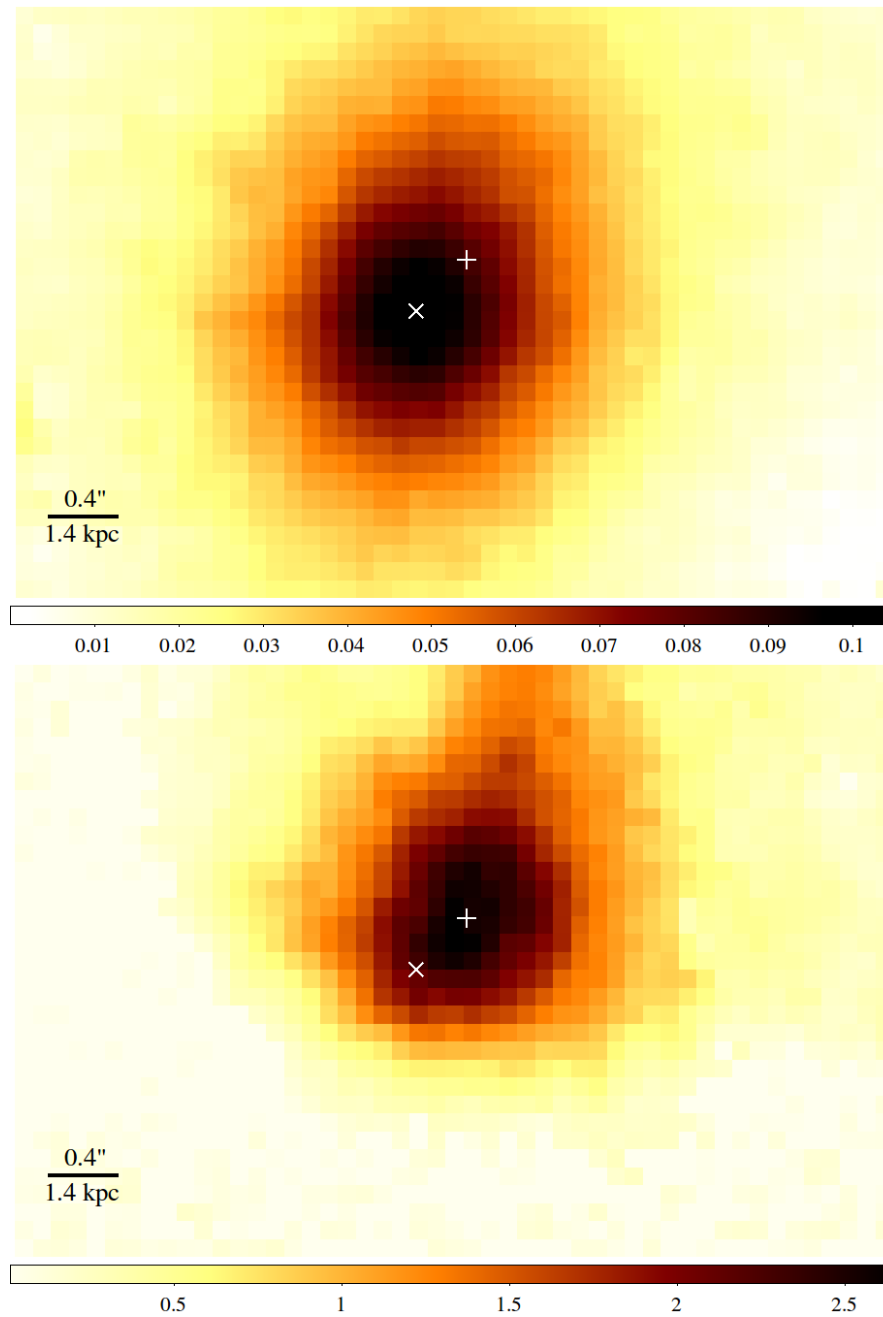


Figure 7.3: Maps of the continuum (top) and H $\alpha$  flux (bottom) in units of  $10^{-17} \text{ erg cm}^{-2} \text{ s}^{-1} \text{ \AA}^{-1}$  and  $10^{-17} \text{ erg cm}^{-2} \text{ s}^{-1}$ , respectively. The 'x' marks the continuum centroid and the '+' marks the H $\alpha$  flux centroid.

et al. (2009). The  $H\alpha$  flux centroid is offset with respect to the continuum centroid by 0.4 arcsec (1.4 kpc) to the northwest. Following the classification scheme of Hamer et al. (in prep), MS0735 falls into the category of a 'plume', which is characterized by extended  $H\alpha$  emission in one preferential direction that is not shared by the continuum and a small offset between the peak in  $H\alpha$  and continuum emission. The cause of this plume is not yet known. The radio jets are oriented toward the northeast and southwest, so entrainment in either the jet or a rising bubble from the rejuvenated outburst cannot be responsible for the plume.

Figure 7.4 shows the velocity map of the  $H\alpha$  nebula in units of  $\text{km s}^{-1}$ . Ranging between  $-100$  and  $250 \text{ km s}^{-1}$ , the top panel shows the velocity structure of the entire nebula. Blueshifted emission at  $-100 \text{ km s}^{-1}$  is observed 2.6 kpc to the southwest of the continuum and  $H\alpha$  centroids. Moving across the centre, the velocity steadily increases until it reaches  $\sim 80 \text{ km s}^{-1}$  4.2 kpc to the northeast of the centroids. This velocity component is shown in the bottom panel of Figure 7.4 (rescaled version of the top panel), and appears to be separate from the velocity component to the northwest. Contours of  $H\alpha$  flux are overlaid on the image, and indicate that the velocity gradient across the centre is of lower flux than the emission extending to the north. This ordered motion is discussed further in section 7.5.

The velocity component toward the northwest is redshifted by  $100 - 250 \text{ km s}^{-1}$  relative to the systemic velocity of the BCG. This component is coincident with the offset between the  $H\alpha$  and continuum centroids, and is roughly aligned with the contours of  $H\alpha$  flux. We therefore attribute this velocity component to the plume discussed previously. Why the largest velocities are observed along the exterior of the plume is not clear. In the future this component will need to be studied in greater detail.

Shown in Figure 7.5, the map of velocity dispersion peaks where the ordered motion and plume overlap. This may be caused by an interaction between the plume and the ordered motion. The source of the plume may disrupt the ordered motion, dragging some of the blueshifted gas toward the north and increasing the velocity dispersion. Alternatively, the two velocity components may be spatially separate with projection along the line-of-sight leading to the increase in observed velocity dispersion. These two possibilities can be distinguished by fitting the  $H\alpha$  line with two Gaussians, one for each velocity component. An improvement in the fit would then indicate that the plume and ordered motion are spatially separated.

## 7.5 Ordered Motion

A clear velocity gradient is observed across the flux centroids, and is indicative of ordered motion in the gaseous nebula. A velocity profile, shown in Figure 7.6, was created by extracting velocity

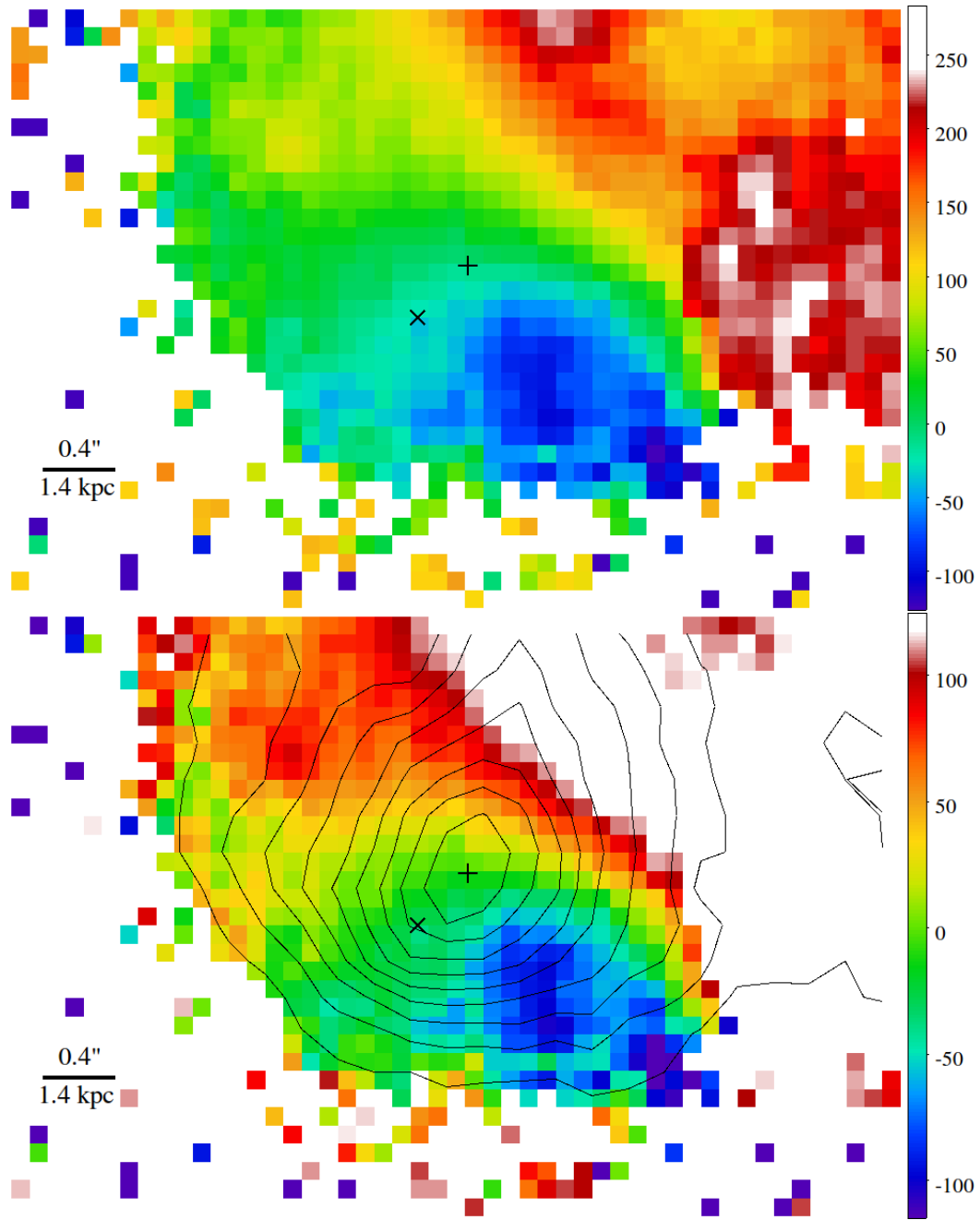


Figure 7.4: Maps of H $\alpha$  velocity, in units of  $\text{km s}^{-1}$ . The 'x' marks the continuum centroid and the '+' marks the H $\alpha$  flux centroid. All velocity structure in the BCG is shown in the top map, with only the ordered motion shown in the bottom along with contours of H $\alpha$  flux.

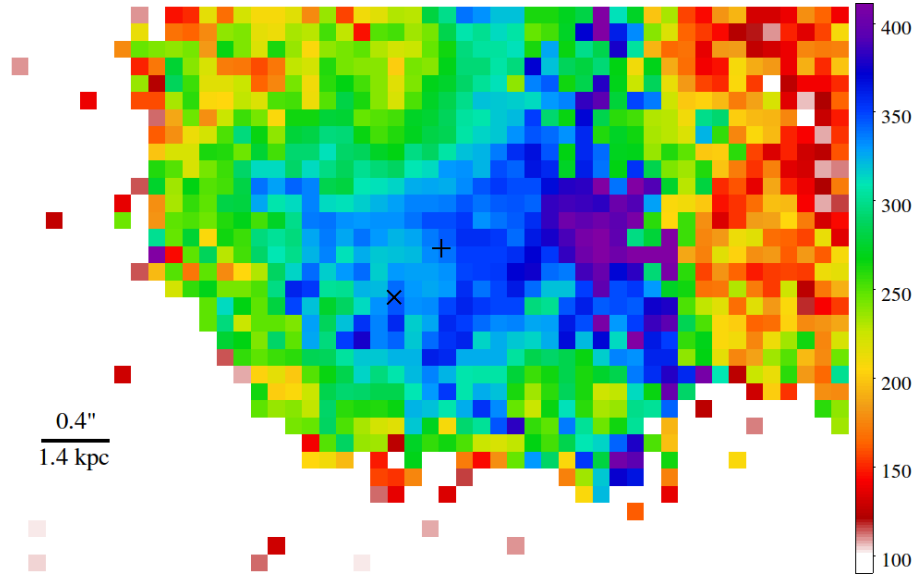


Figure 7.5: Map of velocity dispersion in units of  $\text{km s}^{-1}$ . The ‘ $\times$ ’ marks the continuum centroid and the ‘+’ marks the  $\text{H}\alpha$  flux centroid.

in 0.1 arcsec intervals along a 3 arcsec slit oriented  $45^\circ$  east of north, averaging over its 0.3 arcsec width. Toward the northeast the velocity peaks at  $+85 \text{ km s}^{-1}$  at a distance of 1.1 arcsec (4 kpc) from the flux centroid. A blueshifted peak velocity of  $-92 \text{ km s}^{-1}$  is observed 0.7 arcsec (2.5 kpc) southwest of the flux centroid. Separated by a distance of 1.8 arcsec, the velocity maxima give a peak-to-peak velocity of  $\sim 180 \text{ km s}^{-1}$ , corresponding to a velocity gradient of  $\Delta v/\Delta r \approx 30 \text{ km s}^{-1} \text{ kpc}^{-1}$ . If this gradient corresponds to rotation, then an inclination correction will need to be made. Zero-velocity emission, indicated by the solid lines in Figure 7.6, is offset from the flux and continuum centroids by  $\sim 0.13$  arcsec to the northeast.

### 7.5.1 Rotation

A large fraction of the Hamer et al. (in prep) sample contain a velocity gradient that is consistent with rotation about the nucleus of the BCG. This rotation may correspond to a disk that formed from gas cooling out of the ICM, which would serve as a fuel reservoir for future AGN outbursts. This is the case for Hydra A, where the dynamics of the cold gas reveal a massive, rotating disk 5 kpc in diameter (Hamer et al., 2014). The velocity profile of a rotating disk can be approximated

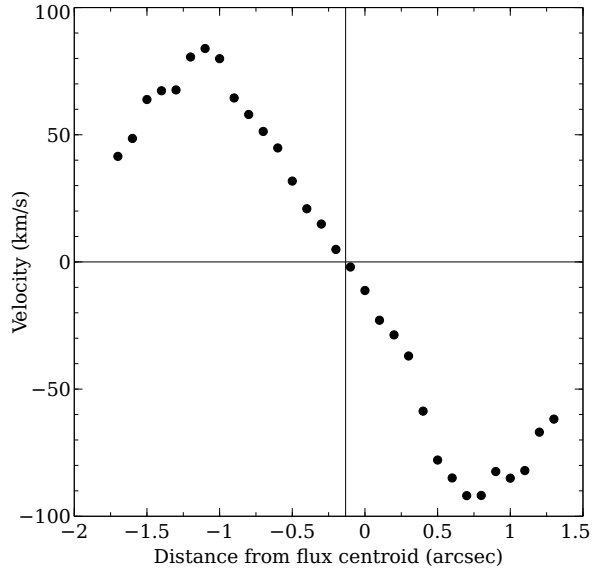


Figure 7.6: Velocity gradient of the H $\alpha$  nebula, determined by averaging the velocities within a 0.3 arcsec wide slit, oriented 45° east from north.

by an arctan function (Courteau, 1997)

$$v(r) = v_0 + \frac{2}{\pi} v_c \arctan(R), \quad (7.5)$$

where  $R = (r - r_0)/r_t$ ,  $v_0$  is the velocity centre of rotation,  $r_0$  is the spatial centre of the galaxy,  $v_c$  is the asymptotic velocity, and  $r_t$  is the radius at which the curve transitions from rising to flat. However, the observed velocity profile turns over at large radii instead of plateauing, so an arctan function does not provide a reasonable fit to Figure 7.6.

Between  $-1$  and  $0.75$  arcsec the velocity gradient is relatively linear, possibly corresponding to solid body rotation. Since  $v = \sqrt{GM/r} \propto r$  in this region, the density of the disk,  $\rho = M/V$  is constant. Including a correction for the inclination of the disk,  $i$ , the disk velocity is given by

$$v_{\text{obs}} = \sqrt{\frac{GM}{R}} \sin i. \quad (7.6)$$

For an edge on Keplerian disk, the velocity 3 kpc away from a  $5 \times 10^9 M_\odot$  black hole is 85 km/s, which is slightly smaller than the observed velocity maximum of 90 km/s. While this may be consistent with the observations, the minor axis of the disk is nearly equal in size to the major axis, so it is unlikely that the disk is edge on. Alternatively, the observed velocity maximum is

consistent with a Keplerian disk in orbit around an ultramassive black hole of mass  $7 \times 10^{10} M_{\odot}$  at an inclination of  $17^{\circ}$  to the line of sight. A circular disk with this inclination has a major-to-minor axis ratio of 1.05, which is roughly consistent with observations.

Interpreting the observed velocity gradient as a disk has a number of issues. First, the majority of the gas in MS0735 is not contained in the structure with the velocity gradient. The flux contours overlaid on Figure 7.4 (bottom) show that the bright emission extends to the north, with fainter emission filling the velocity gradient. A rotating disk should serve as the reservoir of gas cooling out of the ICM, and would therefore comprise the majority of the nebula’s mass. The low flux of the high velocity ends of the velocity gradient suggests that this ordered motion is the result of something other than a disk. Additionally, the maximum blueshifted velocity lies closer to the  $H\alpha$  flux centroid than the maximum redshifted velocity, indicating that the disk is not symmetric about the central black hole. If this structure is a disk, then either the flux centroid or the disk itself is not centred on the ultramassive black hole. Finally, disks are associated with high rates of star formation. For example, Hydra A contains an edge on disk that is 5 kpc in diameter and is forming stars at a rate of  $2 - 3 M_{\odot} \text{ yr}^{-1}$  (Donahue et al., 2011; Hoffer et al., 2012). The lack of evidence for star formation in the BCG of MS0735 opposes the interpretation of a stable disk.

## 7.5.2 Entrainment

A velocity gradient could also be produced if the gas is being dragged away from the nucleus. The radio jets in MS0735 are aligned with the velocity gradient, suggesting that entrainment may be responsible for creating the observed velocity gradient. This interpretation is consistent with the morphology of the flux, which decreases toward the high velocity ends of the gradient. Entrainment would couple to only a small fraction of the gas reservoir, accumulating more gas over time and naturally leading to a lower flux at large radii. The turn-over in the velocity profile can be understood as the gas disconnecting from the jet and falling back toward the BCG. Reaching velocities of only  $\pm 90 \text{ km s}^{-1}$ , much smaller than the  $\sim 600 \text{ km s}^{-1}$  of the rising bubbles, the jet must be located near the plane of the sky. A significant inclination in the relativistic jet would cause one end of the jet to be beamed away from our line of sight, manifesting as a single-ended jet. A bipolar jet is observed in MS0735, indicating that the jet does lie near the plane of the sky, so the small velocities are to be expected.

A reliable interpretation of the velocity structure must explain all of its constituents. Each of these explanations fails to account for the velocity structure of the plume, the origin of which is currently not understood. Although we treated the velocity gradient as an isolated system in our discussion, it is still connected to the plume. Redshifted emission at  $80 - 100 \text{ km s}^{-1}$  extends

along the northwestern edge of the structure shown in Figure 7.4 (bottom), where the velocity gradient is in contact with the plume. This interaction may correspond to a shear in the ordered motion along the direction of the plume, though it is not clear if this is the case. Since the origin of both velocity components is currently not understood, no firm conclusion may be drawn at this time. We may only suggest that the velocity gradient is caused by entrainment in the radio jets.

## 7.6 Motion Induced by an Ultramassive Black Hole

The possibility that MS0735 hosts an ultramassive black hole with a mass of  $\sim 7 \times 10^{10} M_{\odot}$  was first suggested by McNamara et al. (2009). A black hole of mass  $M_{BH}$  has a gravitational radius of influence of

$$\frac{R_g}{\text{kpc}} \approx 0.25 \left( \frac{M_{BH}}{10^{10} M_{\odot}} \right) \left( \frac{\sigma}{400 \text{ km s}^{-1}} \right)^{-2}, \quad (7.7)$$

where  $\sigma$  is the stellar velocity dispersion well beyond  $R_g$ . A  $7 \times 10^{10} M_{\odot}$  black hole therefore has a radius of influence of 1.75 kpc (0.5 arcsec), which is comparable to the radius of the seeing in our observations. If the larger-scale motion can be modelled accurately, then a measurement of the velocity dispersion within the black hole's radius of influence would provide a direct measurement of black hole mass.

In practice the highly uncertain origin of the velocity components will make it very difficult to model the velocity structure of the  $H\alpha$  nebula. As a result, it is unlikely that a black hole mass will be obtained from these data. Furthermore, with a seeing 0.8 arcsec in diameter, the minimum black hole mass that would be detectable is  $6 \times 10^{10} M_{\odot}$ . Even if MS0735 does host an unusually large black hole, it cannot be detected unless its mass approaches  $10^{11} M_{\odot}$ . While the stellar velocity dispersion of the BCG may be closer to  $300 \text{ km s}^{-1}$ , which increases the radius of influence to 3 kpc (0.9 arcsec), the non-gravitational motion induced by the radio jet would likely still prevent the detection of motion induced by the black hole.

## 7.7 Mass Estimates

$H\alpha$  line emission originates from the recombination of protons and electrons in the photoionized skins of gaseous nebulae. The mass of the ionized gas in the nebula, which represents a small fraction of the total gas mass, is given by

$$M_i = \frac{m_p}{\alpha_B n_e} \frac{L_{H\alpha}}{h\nu} = 5.3 \times 10^6 \left( \frac{n_e}{200 \text{ cm}^{-3}} \right)^{-1} \left( \frac{L_{H\alpha}}{10^{42} \text{ erg s}^{-1}} \right) M_{\odot}, \quad (7.8)$$

where  $\alpha_B = 2.59 \times 10^{-13} \text{ cm}^3 \text{ s}^{-1}$  is the recombination coefficient and  $L/h\nu$  is the number of ionizing photons per second.

A degenerate combination of electron density,  $n_e$ , and temperature,  $T$ , in units of  $n_e(10^4/T)^{1/2}$  can be determined from the intensity ratio  $[\text{SII}]\lambda 6716/\lambda 6731$  (Osterbrock & Ferland, 2006). Fitting the two  $[\text{SII}]$  lines in Figure 7.1 simultaneously yields a  $[\text{SII}]\lambda 6716$  flux of  $1.8 \times 10^{-16} \text{ erg cm}^{-2} \text{ s}^{-1}$ , a  $[\text{SII}]\lambda 6731$  flux of  $1.5 \times 10^{-16} \text{ erg cm}^{-2} \text{ s}^{-1}$ , and an intensity ratio of 1.2. This intensity ratio corresponds to a density of  $n_e(10^4/T)^{1/2} \approx 200 \text{ cm}^{-3}$ . Assuming pressure balance with the X-ray emitting gas within 10 kpc allows the degeneracy between density and temperature to be removed. From Figure 3.4, the central deprojected electron density is  $4.9 \times 10^{-2} \text{ cm}^{-3}$  and the temperature is  $3.4 \text{ keV} = 3.9 \times 10^7 \text{ K}$ . Combining this with the previous result gives a nebular temperature of  $9.7 \times 10^3 \text{ K} \approx 10^4 \text{ K}$ , so the electron density of the gaseous nebula is  $200 \text{ cm}^{-3}$ .

Within a 1 arcsec (3.5 kpc) radius from the  $\text{H}\alpha$  flux centroid the total  $\text{H}\alpha$  flux is  $4.7 \times 10^{-15} \text{ erg cm}^{-2} \text{ s}^{-1}$ , corresponding to a luminosity of  $6.4 \times 10^{41} \text{ erg s}^{-1}$  and an ionized gas mass of  $3.4 \times 10^6 M_\odot$ . Edge (2001) and Salomé & Combes (2003) found a correlation between  $\text{H}\alpha$  luminosity and total gas mass deduced from observations of CO lines. With a molecular gas mass of  $< 3 \times 10^9 M_\odot$  within the central 50 kpc of the BCG (Salomé & Combes, 2008), the corresponding  $\text{H}\alpha$  luminosity is  $\sim 7 \times 10^{40} \text{ erg s}^{-1}$ . This falls an order of magnitude below the luminosity measured here, implying that MS0735 hosts an overluminous  $\text{H}\alpha$  nebula. Even a generous upper limit of  $10^{10} M_\odot$  corresponds to an  $\text{H}\alpha$  luminosity ( $\sim 3.5 \times 10^{41} \text{ erg s}^{-1}$ ) that is nearly a factor of two below our measurement.

The excess  $\text{H}\alpha$  luminosity implies that a source of heat is reionizing the nebula. This could arise from recent star formation in excess of the systems analyzed by Salomé & Combes (2003), where a bright  $\text{H}\alpha$  nebula would signify rapid star formation. However, MS0735 is forming stars at a rate of only  $< 0.25 M_\odot \text{ yr}^{-1}$ , so reionization from recent star formation is highly unlikely. Alternatively, AGN heating from the putative shock front associated with the recent outburst may be supplying the extra energy required to reionize the nebula. With an  $[\text{NII}]\lambda 6583/\text{H}\alpha$  line ratio of 1.2, MS0735's BCG lies well above the cut-off of 0.5 that separates HII regions from AGN on Baldwin-Phillips-Terlevich (BPT) diagrams (Osterbrock & Ferland, 2006). Additional spectroscopy of shorter wavelengths is required in order to determine the  $[\text{OIII}]\lambda 5007/\text{H}\beta$  line ratio, which will allow us to discriminate between Seyfert galaxies and Low-Ionization Nuclear Emission-line Regions (LINERs). The low infrared luminosity in MS0735 (Donahue et al., 2011) places it in the LINER regime, implying that AGN heating is required to reionize the nebula.

# Chapter 8

## Conclusions

In this thesis we have presented a detailed analysis of the cool core cluster MS 0735.6+7421. This system hosts cavities exceeding 200 kpc in diameter, making it the most energetic known AGN outburst. Powering such an energetic outburst challenges our understanding of how black holes and their host galaxies co-evolve. Our work focuses mainly on a deep Chandra X-ray observation of MS0735, which allows us to study the full extent of the impact that the powerful radio jet has on the morphology of the ICM. We have also presented preliminary results from integral field spectroscopy obtained with the Gemini Observatory, which maps the spatial and kinematic morphology of ionized gas in the BCG. In this chapter we summarize our key results and outline future work that will be made possible with new or upcoming telescopes.

### 8.1 Summary

Our deep X-ray observation allows us to place new, more accurate constraints on the energetics of the cavities and shock front. Inflating the two large cavities, which have diameters of 200 – 240 kpc, requires a total energy input of  $4pV = 8.8_{-2.4}^{+3.2} \times 10^{61}$  erg. This measurement is consistent with the values reported by Rafferty et al. (2006) and Gitti et al. (2007). Using the sound crossing time, buoyancy time, and refill time, we measure a mean bubble rise time of  $\sim 1.5 \times 10^8$  yr. The mean power output by the AGN is therefore  $1.7_{-0.5}^{+0.6} \times 10^{46}$  erg s<sup>-1</sup>, which exceeds the X-ray luminosity within the cooling radius,  $2.6 \times 10^{44}$  erg s<sup>-1</sup>, by over a factor of 60, so can easily offset radiative losses. Bright rims of cool, dense gas surrounding the cavities are also observed, and correspond to intracluster gas that has been displaced by the bubbles.

A continuous, elliptical shock front encompasses the cavities. Modelling the shock front as a point explosion in an initially hydrostatic, isothermal atmosphere, we find that the surface

brightness profile is best fit by a weak shock with Mach number  $1.26_{-0.09}^{+0.04}$ . This shock injects  $4 \times 10^{61}$  erg into the ICM over a period of  $1.1 \times 10^8$  yr at a mean rate of  $1.1 \times 10^{46}$  erg  $s^{-1}$ . Exceeding the X-ray luminosity by a factor of 40, the power partitioned into the shock front is comparable to the total cavity power and can also offset radiative losses. The difference between shock and cavity ages suggests that our cavity rise times are an overestimate of cavity age, so our cavity power is likely underestimated.

After accounting for projection effects, a Mach 1.26 shock should cause a temperature jump of  $\sim 10\%$ . Our profiles and maps presented in Chapter 3 show a clear temperature jump at the location of the shock front. The mean temperature jump across the shock,  $1.14 \pm 0.07$ , is consistent with the expected jump. Furthermore, we find evidence that the magnitude of the temperature jump varies with position along the shock front. The major axis of the shock has to travel further than the minor axis in the same amount of time, and therefore has a higher Mach number. We find that the temperature jump increases toward the major axis, where the Mach number is highest, and reaches a minimum along the minor axis. While the uncertainties of each measurement are large, the observed trend is clear.

Although the large cavities are easily able to offset radiative losses, we detect pair of cavities corresponding to a more recent AGN outburst. These bubbles are located at a projected distance of 20–25 kpc from the cluster centre, where the outer cavities are no longer able to heat the ICM. The total energy and power of this outburst are  $7.2_{-2.6}^{+3.4} \times 10^{59}$  erg and  $5.2_{-1.8}^{+2.6} \times 10^{44}$  erg  $s^{-1}$ , respectively. With a mean rise time of  $\sim 4.5 \times 10^7$  yr, this outburst indicates that the AGN is rejuvenating on a timescale of  $\sim 1.1 \times 10^8$  yr. Although they are feeble with respect to the outer cavities, the rejuvenated outburst is comparable in size to the bubbles in Perseus and contains sufficient energy to offset radiative losses within the cooling radius. Additionally, a circular feature with a radius of 30 kpc is observed in the hard band surface brightness, and resembles the weak shock front in M87. The associated surface brightness jumps are marginal, so we cannot conclude with certainty if this is, in fact, a shock front. If it is a shock front, it has a Mach number of approximately 1.1 and a mean power of  $4 \times 10^{44}$  erg  $s^{-1}$ .

Cool ( $\sim 3$  keV) gas is observed preferentially along the direction of the radio jets. This corresponds to gas that originated in the cluster nucleus and is being entrained in the radio jet and dragged toward higher altitude. The removal of low entropy gas from the centre of the cluster may play a role in suppressing the condensation of gas out of the ICM and preventing star formation.

Multiphase gas, with temperatures of 3.4 and 0.65 keV, is detected within the central 14 kpc of the cluster. The colder component is 5 times denser than the warmer component, but accounts for only 1% of the mass. Bondi accretion of the colder component is sufficient to power the rejuvenated outburst, but cannot fuel the older, larger AGN outburst. Though cooling at a combined

rate of  $21 M_{\odot} \text{ yr}^{-1}$ , little of this gas condenses out of the intracluster medium. The mean power of the inner cavities is more than enough to offset cooling, though it is not clear if the cavities are able to deposit their energy near the cluster centre. Heating from the putative shock may be responsible for suppressing cooling near the nucleus. Alternatively, entrainment in the radio jet may be removing the gas from the centre and preventing it from cooling.

With the addition of MS0735, we prepare a sample of 10 clusters and groups with multiple generations of cavities. We also include three systems with detected sound waves, two of which overlap with the cavity sample. We find that the outburst interval is shorter than central cooling time in every system. We also compare outburst interval to the heating time, defined as  $4pV/L_X(< r_{\text{cool}})$ . We find that the majority of systems in this analysis have a heating time longer than their outburst interval, implying that AGN cycling is able to continually suppress cooling.

Our preliminary analysis of the  $\text{H}\alpha$  nebula in the BCG of MS0735 reveals a plume of gas that is offset from a region of ordered motion. We find that the ordered component of the velocity structure is inconsistent with a rotating disk. Instead, it is more likely that the gas has been entrained in the radio jet and is being dragged away from the nucleus. However, as we have not yet determined the origin of the plume, we cannot draw any firm conclusions at this time. Using the total luminosity of the  $\text{H}\alpha$  line we measure an ionized gas mass of  $3.4 \times 10^6 M_{\odot}$ , which exceeds the expected gas mass by an order of magnitude and indicates either that atomic gas is not condensing into molecular gas or that a source of heat is reionizing the nebula.

## 8.2 Future Work

From this work it is clear that deep X-ray observations reveal interesting features in cool core clusters. In nearby clusters, filamentary structure and sound waves have also been detected (e.g. Perseus: Fabian et al. 2006, A2052: Blanton et al. 2011). Improving the signal-to-noise ratio in MS0735 by a factor of two would require an additional 1.5 Ms exposure, which is too long to justify the meagre improvement in signal. Instead, advancements must be made by obtaining deep observations of a variety of clusters. This direction is critical to extend our work on the time interval between AGN outbursts.

Future observations hold exciting prospects for improving our understanding of AGN feedback. The next major advance in X-ray astronomy will come in late 2015 with the launch of ASTRO-H. At the cost of spatial resolution, the microcalorimeter on ASTRO-H will be able to study the hot atmosphere in galaxy clusters with unprecedented spectral resolution (Takahashi et al., 2012). This high-resolution spectroscopy will reveal the non-thermal motion in the cores of clusters. Bubbles, weak shocks, and sound waves all contribute to a complex velocity struc-

ture in the ICM. Understanding how this motion is dissipated is crucial in determining how AGN feedback heats the ICM and suppresses cooling.

Early Science observations with the Atacama Large Millimeter Array (ALMA), which began in 2012, have already led to interesting advances in radio astronomy. ALMA is able to map the molecular gas supply in BCGs with an unprecedented combination of spatial and spectral resolution. Observations of the BCGs in A1664 (Russell et al., 2014) and A1835 (McNamara et al., 2014) have revealed massive outflows of molecular gas trailing the buoyantly rising bubbles, implying that the dense molecular gas environments are being efficiently coupled to and uplifted by the tenuous bubbles. Upcoming observations of additional galaxy clusters will show how wide-spread this effect is.

ALMA also presents the interesting prospect of detecting X-ray cavities using the Sunyaev-Zel'dovich (SZ) effect. Isolating the contribution of relativistic particles to the SZ signal will allow for the measurement of non-thermal pressure within a cavity (Prokhorov et al., 2010). These studies will show conclusively if bubbles are in pressure balance with the surrounding plasma. Unfortunately, MS0735 resides too far north to be observed with ALMA.

# APPENDICES

# Appendix A

## Other Contributions

During my M.Sc. I have been involved in a number of other projects, including several publications and some proposals. My contributions to these papers are outlined below.

1. *A  $10^{10}$  Solar Mass Flow of Molecular Gas in the A1835 Brightest Cluster Galaxy*, McNamara, B. R.; Russell, H. R.; Nulsen, P. E. J.; Edge, A. C.; Murray, N. W.; Main, R. A.; Vantyghem, A. N.; Combes, F.; Fabian, A. C.; Salome, P.; Kirkpatrick, C. C.; Baum, S. A.; Bregman, J. N.; Donahue, M.; Egami, E.; Hamer, S.; O’Dea, C. P.; Oonk, J. B. R.; Tremblay, G.; Voit, G. M., 2014, *ApJ*, 785, 44.

This paper presents an analysis of an Early Science ALMA observation of the BCG in A1835. I was involved in the early steps of the data processing, which included creating maps of flux and velocity to be used for additional ALMA proposals. I also participated in the discussion of the results and provided constructive comments on drafts of the paper.

2. *Massive Molecular Gas Flows in the A1664 Brightest Cluster Galaxy*, Russell, H. R.; McNamara, B. R.; Edge, A. C.; Nulsen, P. E. J.; Main, R. A.; Vantyghem, A. N.; Combes, F.; Fabian, A. C.; Murray, N.; Salom, P.; Wilman, R. J.; Baum, S. A.; Donahue, M.; O’Dea, C. P.; Oonk, J. B. R.; Tremblay, G. R.; Voit, G. M., 2014, *ApJ*, 754, 78.

This is a sister paper to McNamara et al. (2014), presenting results from an ALMA observation of the BCG in A1664. As such, my contribution to this paper is the same as in McNamara et al. (2014): I created early flux and velocity maps, participated in the discussion of the results, and helped proofread the paper.

3. *Radiative efficiency, variability and Bondi accretion on to massive black holes: the transition from radio AGN to quasars in brightest cluster galaxies*, Russell, H. R.; McNamara,

B. R.; Edge, A. C.; Hogan, M. T.; Main, R. A.; Vantghem, A. N., 2013, MNRAS, 432, 530-553.

This paper studies the unresolved X-ray point sources at the centres of clusters using data from the Chandra X-ray observatory. I assisted in proofreading the draft of this paper.

# References

- Anders E., Grevesse N., 1989, *Geochim. Cosmochim. Acta*, 53, 197
- Arnaud K. A., 1996, in Jacoby G. H., Barnes J., eds, *Astronomical Data Analysis Software and Systems V* Vol. 101 of *Astronomical Society of the Pacific Conference Series*, *XSPEC: The First Ten Years*. p. 17
- Arnaud M., 2005, in Melchiorri F., Rephaeli Y., eds, *Background Microwave Radiation and Intracluster Cosmology X-ray observations of clusters of galaxies*. p. 77
- Balucinska-Church M., McCammon D., 1992, *ApJ*, 400, 699
- Begelman M. C., 2004, *Coevolution of Black Holes and Galaxies*, p. 374
- Bîrzan L., McNamara B. R., Nulsen P. E. J., Carilli C. L., Wise M. W., 2008, *ApJ*, 686, 859
- Bîrzan L., Rafferty D. A., McNamara B. R., Wise M. W., Nulsen P. E. J., 2004, *ApJ*, 607, 800
- Bîrzan L., Rafferty D. A., Nulsen P. E. J., McNamara B. R., Röttgering H. J. A., Wise M. W., Mittal R., 2012, *MNRAS*, 427, 3468
- Blandford R. D., Rees M. J., 1974, *MNRAS*, 169, 395
- Blanton E. L., Randall S. W., Clarke T. E., Sarazin C. L., McNamara B. R., Douglass E. M., McDonald M., 2011, *ApJ*, 737, 99
- Blanton E. L., Randall S. W., Douglass E. M., Sarazin C. L., Clarke T. E., McNamara B. R., 2009, *ApJ*, 697, L95
- Blanton E. L., Sarazin C. L., McNamara B. R., Wise M. W., 2001, *ApJ*, 558, L15
- Böhringer H., Matsushita K., Churazov E., Ikebe Y., Chen Y., 2002, *A&A*, 382, 804

Bondi H., 1952, MNRAS, 112, 195

Burbidge G. R., 1956, ApJ, 124, 416

Canning R. E. A., Sun M., Sanders J. S., Clarke T. E., Fabian A. C., Giacintucci S., Lal D. V., Werner N., Allen S. W., Donahue M., Edge A. C., Johnstone R. M., Nulsen P. E. J., Salomé P., Sarazin C. L., 2013, MNRAS

Cavagnolo K. W., Donahue M., Voit G. M., Sun M., 2009, ApJS, 182, 12

Cavaliere A., Fusco-Femiano R., 1976, A&A, 49, 137

Churazov E., Brüggén M., Kaiser C. R., Böhringer H., Forman W., 2001, ApJ, 554, 261

Churazov E., Forman W., Jones C., Böhringer H., 2000, A&A, 356, 788

Churazov E., Sunyaev R., Forman W., Böhringer H., 2002, MNRAS, 332, 729

Clowe D., Bradač M., Gonzalez A. H., Markevitch M., Randall S. W., Jones C., Zaritsky D., 2006, ApJ, 648, L109

Clowe D., Gonzalez A., Markevitch M., 2004, ApJ, 604, 596

Courteau S., 1997, AJ, 114, 2402

David L. P., Nulsen P. E. J., 2008, ApJ, 689, 837

David L. P., Nulsen P. E. J., McNamara B. R., Forman W., Jones C., Ponman T., Robertson B., Wise M., 2001, ApJ, 557, 546

De Grandi S., Ettori S., Longhetti M., Molendi S., 2004, A&A, 419, 7

De Grandi S., Molendi S., 2001, ApJ, 551, 153

de Grandi S., Molendi S., 2009, A&A, 508, 565

De Young D. S., 2003, MNRAS, 343, 719

De Young D. S., 2006, ApJ, 648, 200

Donahue M., de Messières G. E., O'Connell R. W., Voit G. M., Hoffer A., McNamara B. R., Nulsen P. E. J., 2011, ApJ, 732, 40

Donahue M., Stocke J. T., Gioia I. M., 1992, ApJ, 385, 49

Dunn R. J. H., Fabian A. C., 2006, MNRAS, 373, 959

Dunn R. J. H., Fabian A. C., Taylor G. B., 2005, MNRAS, 364, 1343

Edge A. C., 2001, MNRAS, 328, 762

Edge A. C., Stewart G. C., 1991, MNRAS, 252, 414

Edge A. C., Stewart G. C., Fabian A. C., Arnaud K. A., 1990, MNRAS, 245, 559

Fabian A. C., 1994, ARA&A, 32, 277

Fabian A. C., 2012, ARA&A, 50, 455

Fabian A. C., Johnstone R. M., Sanders J. S., Conselice C. J., Crawford C. S., Gallagher III J. S., Zweibel E., 2008, Nat, 454, 968

Fabian A. C., Reynolds C. S., Taylor G. B., Dunn R. J. H., 2005, MNRAS, 363, 891

Fabian A. C., Sanders J. S., Ettori S., Taylor G. B., Allen S. W., Crawford C. S., Iwasawa K., Johnstone R. M., Ogle P. M., 2000, MNRAS, 318, L65

Fabian A. C., Sanders J. S., Taylor G. B., Allen S. W., Crawford C. S., Johnstone R. M., Iwasawa K., 2006, MNRAS, 366, 417

Forman W., Jones C., Churazov E., Markevitch M., Nulsen P., Vikhlinin A., Begelman M., Böhringer H., Eilek J., Heinz S., Kraft R., Owen F., Pahre M., 2007, ApJ, 665, 1057

Freeman P. E., Kashyap V., Rosner R., Lamb D. Q., 2002, ApJS, 138, 185

Giacconi R., Murray S., Gursky H., Kellogg E., Schreier E., Tananbaum H., 1972, ApJ, 178, 281

Gitti M., McNamara B. R., Nulsen P. E. J., Wise M. W., 2007, ApJ, 660, 1118

Gitti M., Nulsen P. E. J., David L. P., McNamara B. R., Wise M. W., 2011, ApJ, 732, 13

Gursky H., Schwartz D. A., 1977, ARA&A, 15, 541

Hamer S. L., Edge A. C., Swinbank A. M., Oonk J. B. R., Mittal R., McNamara B. R., Russell H. R., Bremer M. N., Combes F., Fabian A. C., Nesvadba N. P. H., O’Dea C. P., Baum S. A., Salomé P., Tremblay G., Donahue M., Ferland G. J., Sarazin C. L., 2014, MNRAS, 437, 862

Hardcastle M. J., Evans D. A., Croston J. H., 2007, MNRAS, 376, 1849

- Hartmann D., Burton W. B., 1997, Atlas of Galactic Neutral Hydrogen. Cambridge University Press
- Hoffer A. S., Donahue M., Hicks A., Barthelemy R. S., 2012, ApJS, 199, 23
- Hudson D. S., Mittal R., Reiprich T. H., Nulsen P. E. J., Andernach H., Sarazin C. L., 2010, A&A, 513, A37
- Johnstone R. M., Fabian A. C., Nulsen P. E. J., 1987, MNRAS, 224, 75
- Kalberla P. M. W., Burton W. B., Hartmann D., Arnal E. M., Bajaja E., Morras R., Pöppel W. G. L., 2005, A&A, 440, 775
- Kellogg E., Gursky H., Leong C., Schreier E., Tananbaum H., Giacconi R., 1971, ApJ, 165, L49
- Kellogg E., Murray S., Giacconi R., Tananbaum T., Gursky H., 1973, ApJ, 185, L13
- Kirkpatrick C. C., Gitti M., Cavagnolo K. W., McNamara B. R., David L. P., Nulsen P. E. J., Wise M. W., 2009, ApJ, 707, L69
- Kirkpatrick C. C., McNamara B. R., Rafferty D. A., Nulsen P. E. J., Bîrzan L., Kazemzadeh F., Wise M. W., Gitti M., Cavagnolo K. W., 2009, ApJ, 697, 867
- Kormendy J., Bender R., 2009, ApJ, 691, L142
- Lauer T. R., Faber S. M., Richstone D., Gebhardt K., Tremaine S., Postman M., Dressler A., Aller M. C., Filippenko A. V., Green R., Ho L. C., Kormendy J., Magorrian J., Pinkney J., 2007, ApJ, 662, 808
- Liedahl D. A., Osterheld A. L., Goldstein W. H., 1995, ApJ, 438, L115
- Machacek M. E., Jerius D., Kraft R., Forman W. R., Jones C., Randall S., Giacintucci S., Sun M., 2011, ApJ, 743, 15
- McCarthy I. G., Babul A., Bower R. G., Balogh M. L., 2008, MNRAS, 386, 1309
- McNamara B. R., Kazemzadeh F., Rafferty D. A., Bîrzan L., Nulsen P. E. J., Kirkpatrick C. C., Wise M. W., 2009, ApJ, 698, 594
- McNamara B. R., Nulsen P. E. J., 2007, ARA&A, 45, 117
- McNamara B. R., Nulsen P. E. J., 2012, New Journal of Physics, 14, 055023

McNamara B. R., Nulsen P. E. J., Wise M. W., Rafferty D. A., Carilli C., Sarazin C. L., Blanton E. L., 2005, *Nat*, 433, 45

McNamara B. R., O'Connell R. W., 1989, *AJ*, 98, 2018

McNamara B. R., Rohanizadegan M., Nulsen P. E. J., 2011, *ApJ*, 727, 39

McNamara B. R., Russell H. R., Nulsen P. E. J., Edge A. C., Murray N. W., Main R. A., Vantghem A. N., et al. 2014, *ApJ*, 785, 44

McNamara B. R., Wise M., Nulsen P. E. J., David L. P., Sarazin C. L., Bautz M., Markevitch M., Vikhlinin A., Forman W. R., Jones C., Harris D. E., 2000, *ApJ*, 534, L135

Meier D. L., 1999, *ApJ*, 522, 753

Meier D. L., 2001, *ApJ*, 548, L9

Mewe R., Gronenschild E. H. B. M., van den Oord G. H. J., 1985, *A&AS*, 62, 197

Mewe R., Lemen J. R., van den Oord G. H. J., 1986, *A&AS*, 65, 511

Mitchell R. J., Culhane J. L., Davison P. J. N., Ives J. C., 1976, *MNRAS*, 175, 29P

Mushotzky R. F., Serlemitsos P. J., Boldt E. A., Holt S. S., Smith B. W., 1978, *ApJ*, 225, 21

Nulsen P. E. J., David L. P., McNamara B. R., Jones C., Forman W. R., Wise M., 2002, *ApJ*, 568, 163

Nulsen P. E. J., Hambrick D. C., McNamara B. R., Rafferty D., Birzan L., Wise M. W., David L. P., 2005, *ApJ*, 625, L9

Nulsen P. E. J., Li Z., Forman W. R., Kraft R. P., Lal D. V., Jones C., Zhuravleva I., Churazov E., Sanders J. S., Fabian A. C., Johnson R. E., Murray S. S., 2013, *ApJ*, 775, 117

Nulsen P. E. J., McNamara B. R., Wise M. W., David L. P., 2005, *ApJ*, 628, 629

O'Dea C. P., 1985, *ApJ*, 295, 80

O'Dea C. P., Baum S. A., Mack J., Koekemoer A. M., Laor A., 2004, *ApJ*, 612, 131

Osterbrock D. E., Ferland G. J., 2006, *Astrophysics of gaseous nebulae and active galactic nuclei*

Panagoulia E. K., Fabian A. C., Sanders J. S., 2014, *MNRAS*, 438, 2341

Peres C. B., Fabian A. C., Edge A. C., Allen S. W., Johnstone R. M., White D. A., 1998, MNRAS, 298, 416

Peterson J. R., Fabian A. C., 2006, Phys. Rep., 427, 1

Peterson J. R., Kahn S. M., Paerels F. B. S., Kaastra J. S., Tamura T., Bleeker J. A. M., Ferrigno C., Jernigan J. G., 2003, ApJ, 590, 207

Proga D., Begelman M. C., 2003, ApJ, 592, 767

Prokhorov D. A., Antonuccio-Delogu V., Silk J., 2010, A&A, 520, A106

Rafferty D. A., Bîrzan L., Nulsen P. E. J., McNamara B. R., Brandt W. N., Wise M. W., Röttgering H. J. A., 2013, MNRAS, 428, 58

Rafferty D. A., McNamara B. R., Nulsen P. E. J., 2008, ApJ, 687, 899

Rafferty D. A., McNamara B. R., Nulsen P. E. J., Wise M. W., 2006, ApJ, 652, 216

Randall S. W., Forman W. R., Giacintucci S., Nulsen P. E. J., Sun M., Jones C., Churazov E., David L. P., Kraft R., Donahue M., Blanton E. L., Simionescu A., Werner N., 2011, ApJ, 726, 86

Rebusco P., Churazov E., Böhringer H., Forman W., 2005, MNRAS, 359, 1041

Rebusco P., Churazov E., Böhringer H., Forman W., 2006, MNRAS, 372, 1840

Reiprich T. H., Böhringer H., 2002, ApJ, 567, 716

Reynolds C. S., McKernan B., Fabian A. C., Stone J. M., Vernaleo J. C., 2005, MNRAS, 357, 242

Russell H. R., McNamara B. R., Edge A. C., Nulsen P. E. J., Main R. A., Vantyghem A. N., Combes F., Fabian A. C., Murray N., Salomé P., Wilman R. J., Baum S. A., Donahue M., O’Dea C. P., Oonk J. B. R., Tremblay G. R., Voit G. M., 2014, ApJ, 784, 78

Russell H. R., Sanders J. S., Fabian A. C., 2008, MNRAS, 390, 1207

Salomé P., Combes F., 2003, A&A, 412, 657

Salomé P., Combes F., 2008, A&A, 489, 101

Sanders J. S., 2006, MNRAS, 371, 829

Sanders J. S., Fabian A. C., 2007, MNRAS, 381, 1381

Sanders J. S., Fabian A. C., 2008, MNRAS, 390, L93

Sarazin C. L., 1988, X-ray emission from clusters of galaxies

Saripalli L., Subrahmanyam R., Udaya Shankar N., 2002, ApJ, 565, 256

Schoenmakers A. P., de Bruyn A. G., Röttgering H. J. A., van der Laan H., Kaiser C. R., 2000, MNRAS, 315, 371

Serlemitsos P. J., Smith B. W., Boldt E. A., Holt S. S., Swank J. H., 1977, ApJ, 211, L63

Simionescu A., Werner N., Böhringer H., Kaastra J. S., Finoguenov A., Brüggem M., Nulsen P. E. J., 2009, A&A, 493, 409

Stoche J. T., Morris S. L., Gioia I. M., Maccacaro T., Schild R., Wolter A., Fleming T. A., Henry J. P., 1991, ApJS, 76, 813

Takahashi T., Mitsuda K., Kelley R., Aarts H., Aharonian F., Akamatsu H., Akimoto F., Allen S., et al. 2012, in Society of Photo-Optical Instrumentation Engineers (SPIE) Conference Series Vol. 8443 of Society of Photo-Optical Instrumentation Engineers (SPIE) Conference Series, The ASTRO-H X-ray Observatory

Vantyghe A. N., McNamara B. R., Russell H. R., Main R. A., Nulsen P. E. J., Wise M. W., Hoekstra H., Gitti M., 2014, MNRAS, 442, 3192

Vikhlinin A., Markevitch M., Murray S. S., Jones C., Forman W., Van Speybroeck L., 2005, ApJ, 628, 655

Voigt L. M., Fabian A. C., 2004, MNRAS, 347, 1130

Voit G. M., Donahue M., 2005, ApJ, 634, 955

Werner N., Durret F., Ohashi T., Schindler S., Wiersma R. P. C., 2008, Space Sci. Rev., 134, 337

White D. A., Fabian A. C., Allen S. W., Edge A. C., Crawford C. S., Johnstone R. M., Stewart G. C., Voges W., 1994, MNRAS, 269, 589

Wise M. W., McNamara B. R., Nulsen P. E. J., Houck J. C., David L. P., 2007, ApJ, 659, 1153

Wolf M., 1906, Astronomische Nachrichten, 170, 211

Wu K. K. S., Fabian A. C., Nulsen P. E. J., 2000, MNRAS, 318, 889